TECHNISCHE UNIVERSITÄT WIEN
Vienna University of Technology

DIPLOMARBEIT

Dose area product measurements with a novel large area ionization chamber in scanned proton beams

zur Erlangung des akademischen Grades

Diplom-Ingeneurin

im Rahmen des Studiums

Biomedical Engineering

eingereicht von

Sarah Haupt, BSc
Matrikelnummer 1026805

ausgeführt am Atominstitut
der Fakultät für Physik der Technischen Universität Wien

Betreuung
Univ.Prof. Dipl.-Ing. Dr.techn. Dietmar Georg
Mag. Peter Kuess, PhD

Wien, 19. März 2019 _____ _____

Unterschrift Verfasserin Unterschrift Betreuer

Kurzfassung

Technologische Entwicklungen in der Strahlentherapie haben neue Behandlungsmodalitäten wie die intensitätsmodulierte Strahlentherapie mittels hochenergetischer Photonenstrahlung inklusive volumetrischer Arc-Therapie, sowie die Protonen- und Ionenstrahltherapie mittels scanning Technologien vorangetrieben. Diese Entwicklungen bringen einen kontinuierlichen Bedarf nach neuen dosimetrischen Ansätzen und Detektoren mit sich, die geeignet sind genaue Messergebnisse in diesen neuen Modalitäten bei der Verwendung kleiner Felder zu erzielen. Ein Ansatz ist die Verwendung von großflächig lateral integrierenden Ionisationskammern für die Dosimetrie kleiner Strahlenfelder. Dies ist ein vielversprechender Ansatz, da die aktuellen Empfehlungen in der Protonendosimetrie auf Erfahrungen mit passiv gestreuten und modulierten Strahlen beruhen. Hier kann eine Kalibrierung bezüglich der die absorbierte Dosis in Wasser durchgeführt werden. Für gescannte Strahlen ist es praktischer, einen Detektor hinsichtlich der Anzahl der Teilchen oder des dosimetrischen Äquivalents, das heißt des Dosis-Flächen Produkt (DFP) in Wasser, zu kalibrieren. Die Verwendung von Großflächendetektoren mit kleinen Strahlenfeldern würde die übliche Methode von sehr kleinen Detektoren wie p-Typen oder Diamantdetektoren erleichtern. Eine Positionierung der Detektoren gegenüber dem engen Strahl ist beispielsweise für das Dosisflächenprodukt unbedenklich, während sie für kleine Detektoren entscheidend ist.

PTW entwickelte einen Prototyp einer großflächigen Ionisationskammer mit einem aktiven Durchmesser von 147 mm. Im Rahmen dieser Arbeit wird das Verhalten dieses Detektors, welcher weiters als BPC150 bezeichnet wird, in Bezug auf die Protonentherapie untersucht. Die Kammer wird zuerst in einer ^{60}Co Quelle kalibriert.Außerdem wird in einem gescannten Protonenstrahl in der Ionenstrahl-Therapieanlage MedAustron, Wr. Neustadt eine Kreuzkalibrierung (engl.: cross calibration) durchgeführt. Zweidimensionale Ansprechkarten der Kammer unter Verwendung einer Röntgenquelle werden gemessen. Für eine genaue Referenzdosimetrie ist die homogene Reaktion über die gesamte aktive Fläche der Kammer

ist entscheidend. Diese ist aber nicht einfach zu realisieren, da bereits wenige µm-Variationen zwischen der Sammelelektrode und dem Eintrittsfenster zu Ansprechvariationen von mehr als 1% führen. Dosis-Flächen Produkt Messungen unter Verwendung von großen Felder und einzelner kleiner Strahlen werden in einem Protonenstrahl bei verschiedenen Energien durchgeführt. Weitere Messungen mit der Kammer umfassen die Wasseräquivalentdicke sowie das Verhalten in Kohlenstoffstrahlen.

Die Untersuchung der Wasseräquivalentdicke (WET) des BPC150 ergab Ergebnisse von 11,24 mm für die WET der gesamten Kammer und eine WET von 4,63 mm für das Eingangsfenster. Um angemessene Bedingungen sowohl für die Kreuzkalibrierung in Protonenstrahlen als auch für DFP-Messungen mit dem Wide-Field-Ansatz zu gewährleisten, wurde festgestellt, dass eine Feldgröße von 18 cm $\times$ 18 cm ausreichend ist. Die in Photonenstrahlen aufgezeichnete Dosisantwortkarte zeigte eine Variation in der Empfindlichkeit von 4-6% in der Kammermitte. Dies wurde durch Messungen in Protonenstrahlen bestätigt. Messungen in Kohlenstoffionenstrahlen mit dem BPC150 zeigten eine bessere Auflösung des Fragmentationstails im Vergleich zu Kammern mit geringerer aktiver Fläche.

Zusammenfassend ist das Verhalten des BPC150 ähnlich wie bei den PTW-Kammern des Typs 34070. Der größte Unterschied zwischen diesen Kammertypen ist das Antwortverhalten. Die Kammern des Typs PTW34070 zeigen die höchste Empfindlichkeit in der Kammermitte, und die Reaktion nimmt zum Kammerrand allmählich ab, während der BPC150 genau das entgegengesetzte Verhalten zeigt. Der Hauptvorteil der größeren aktiven Fläche liegt in der Messung des Fragmentationstails in leichten Ionenstrahlen.

Abstract

Technological developments in radiation oncology have lead to novel treatment modalities such as intensity modulated radiotherapy with the use of high energy photon beams including arc therapy, as well as proton and ion beam therapy by means of scanning technologies. These developments have created a continuous demand on new dosimetric approaches and new detectors suitable to perform accurate dosimetry for the new modalities. One approach is the use of large-area laterally integrating ionization chambers for the dosimetry of narrow beams. This is a promising approach, as current recommendations in proton dosimetry are based on the experience with passively scattered and modulated beams, where calibration can be performed in terms of absorbed dose to water. For scanned beams it is more practical to calibrate a detector in terms of the number of particles or its dosimetric equivalent the dose are product in water. The use of large area detectors with small beams would relieve the common method of very small detectors such as p-types or diamond detectors. Positioning of the detectors with respect to the narrow beam for example is of no concern for dose area product, while it is crucial for small detectors.

PTW developed a prototype of a large-area ionization chamber with an active diameter of 147 mm. Within the scope of this thesis the behavior of this detector, which will be referred to as BPC150 was investigated, with respect to proton therapy. The chamber was first calibrated in a ^{60}Co source and further cross-calibrate it in a scanned proton beam at MedAustron, the center for ion therapy and research, Wr. Neustadt. Two-dimensional response maps of the chamber, using an X-ray source, were recorded. The homogeneous response over the whole active area of the chamber is crucial for accurate reference dosimetry, but on the other very challenging to realize, as already few µm variations between the collecting electrode and the entrance window result in response variations of more than 1%. Dose area product (DAP) measurements using large fields and single beams were conducted in a proton beam at different energies. Further measurements

with the chamber included its water equivalent thickness as well as its behavior in carbon beams.

The investigation of the water equivalent thickness (WET) of the BPC150 yielded results of 11.24 mm for the WET of the whole chamber and a WET of 4.63 mm for the entrance window. To guarantee adequate conditions for both cross calibration in proton beams and DAP measurements with the broad field approach, a field size of 18 cm $\times$ 18 cm was found to be sufficient. The dose response map recorded in photon beams revealed an under response of 4-6% in the chamber center. This was confirmed by measurements in proton beams. Measurements in carbon ion beams with the BPC150 revealed a better resolution of the fragmentation tail in comparison with chambers with smaller active area.

In summary, the behavior of the BPC150 is very similar to the PTW chambers of type 34070. The real difference between those chamber types are the response behavior. The chambers of type PTW34070 show the highest response in the chamber center and response is gradually decreasing when moving closer to the chamber edge, whereas the BPC150 shows the exact opposite behavior. The major advantage of the larger active area lie in measurements of the fragmentation tail in light ion beams.

Acknowledgements

First, I want to thank Prof. Dr. Dietmar Georg for his supervision of this thesis and for providing me with the ability to work at MedAustron. Getting thirst hand experience with the particle accelerator was very rewarding and unforgettable.

Secondly, I owe my deepest gratitude to my co-supervisor Mag. Peter Kuess, PhD. Our discussions and your support helped to motivate me and to stay enthusiastic throughout my work on the thesis.

I also want to thank DI Dr. Albert Hirtl for recruiting a supervisor for my thesis, Dr. Monika Clausen for showing me the way around MedAustron and DI Hermann Fuchs, PhD for providing me with much needed data.

Moreover, I want to express my profound gratitude to my parents, who made it possible for me to study in the first place, my beloved husband Edward, my sister Teresa, as well as all my friends (you know who you are). Without your love, support and encouragement I would never have come this far!

Contents

1 Introduction

1.1 Motivation

Radiation therapy is one of three main approaches to treat cancer besides surgery and systemic treatments, such as chemo-, hormone- and immunotherapy. The term cancer encompasses a group of diseases, which all have the underlying characteristic of abnormal cell growth with the potential to spread to other parts of the body. Ionizing radiation, which is used during radiation therapy, is generally harmful to the human body, however cancer cells generally have a higher radiosensitivity in comparison with healthy body cells.

Radiation therapy is subdivided into two groups:

- external beam radiation therapy or teletherapy, where the radiation is administered from a source outside of the body
- brachytherapy, where the radiation source is inserted into the patient

Teletherapy with photon radiation is the most common method of radiation therapy used to treat cancer. Besides photons particle radiation can be also be used. Electron beams are beneficial for treating superficial tumors, as their depth dose profile shows a fast build up and afterwards a quick falloff. Proton or carbon ion radiation is advantageous as the show a constant depth dose before the distinct Bragg peak and an almost immediate distant fall off after the maximum. Figure 1.1 shows the depth dose distribution for different types of radiation in water.

Over the last decade research has laid an increasing focus on the usage of small field sizes in radiation therapy. The advantage of small field sizes in radiation therapy lies in the irradiation of only the clinical target volume with little or no over ranging, thus sparing

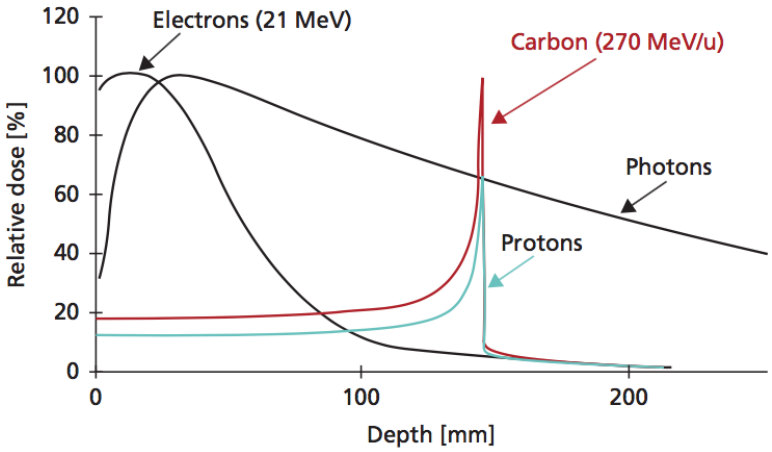

Figure 1.1: *Energy loss per distance in water for different types of radiation; each depth dose curve is normalized to its maximum [1]*

surrounding healthy tissue unnecessary doses. Therefore, a variety of treatment options are becoming more popular and more widely used, as for example:

- intensity modulated radiation therapy, where the intensity of the radiation beam is varied across the tumor volume to provide maximum dose to the tumor and minimal dose to surrounding tissue
- volumetric arc therapy: is an advanced form of intensity modulated radiation therapy, where the dose is delivered to the tumor in one 360° rotation of the treatment machine
- stereotactic radiosurgery: is used for small tumors and a high dose is administered usually in only one session. The treatment units are most commonly a CyberKnife, which is a gantry designed linear accelerator, or a Gamma Knife, which used 201 ^{60}Co sources to aim gamma radiation at a patients brain.
- stereotactic body radiation therapy: stereotactic treatment outside of the cranial region is called stereotactic body radiation therapy

Due to their favorable depth dose distribution, radiation therapy using proton or light ion (usually carbon ions) beams is gaining recognition and more treatment facilities are planned and constructed worldwide. It is thus safe to say that small fields in radiation therapy are increasingly important as is the requirement of consistent reference dosimetry, which becomes more copious the smaller the beam is.

In the following work a new Bragg Peak chamber (further refered to as BPC150), with an active area of 147 mm has been investigated. This work presents the first user tests with this chamber focusing on dose area product (DAP) measurements in proton beams. In general, the BPC150 was until now only investigated by the vendor PTW (PTW Freiburg GmBh, Freiburg, Germany), thus the following examinations are the first done without PTW supervision. The BPC150's intended usage lies in dose and dose rate measurements in proton and heavy ions beams. Thus, the assessment of its performance in such beams, especially for measurements of the DAP, was examined carefully. As ionization chambers have a non-uniform response over their respective active area, this non-uniformity issue was investigated as well. Due to the larger area a higher irregularity could be expected. Preparatory measurements with X-radiation, the DAP measurements and the investigation of the non-uniformity will be discussed in detail in the subsequent chapters. [2] [3] [4]

1.2 Definition and characteristics of ionizing radiation

Ionizing radiation includes both particle (corpuscular) and electromagnetic radiation which is capable of ionizing atoms or molecules. Both the ejection of one or more electrons from the atomic shell, as well as the addition of one or more electrons to a neutral atom, is called ionization.

Essentially, the particle and the photon radiation, as well as the process of direct and indirect ionization are to be distinguished [5] [6]:

- particle radiation consists of particles with rest mass $m_0 > 0$, which may be charged or uncharged, for example: protons (+), electrons (-), neutrons (0), alpha rays (+). In general, a distinction is made between
  1. electron-/positron radiation
  2. particle radiation consisting of heavy charged particles
  3. neutron radiation

  In the medical area particle radiation is mostly used for radiation therapy or nuclear medicine treatments.

- Photon radiation, which is electromagnetic radiation, can lead to ionization due to several interaction processes with matter (which will be explained in detail in the next

section). Frequently, electromagnetic radiation is referred to as gamma radiation when its energy is above a certain threshold (about 10^5 eV). In this work, gamma radiation is only referred to as such if it is produced by a nuclear decay, or annihilation radiation after recombination of an electron-positron pair. X-radiation is further used only for radiation which has its origin in the atomic shell or has arisen due to Coulomb interaction with the nucleus.

Photon radiation is medically used for both diagnostics and therapy. Low energy photons (up to approximately 150 keV) are used in diagnostics. In radiation therapy photons the energies used depend on the depth of the tumor and range from $<$50 keV for contact therapy, between around 80-350 keV for superficial therapy and then up in the MeV region for the treatment of deep seated tumors.

- Direct ionization: Radiation of charged particles (eg, electron or alpha radiation) can lead to direct ionization, because they can interact directly with atoms or molecules of the irradiated material due to their charge, and can ionize by collisions.

- Indirect Ionization: Photon radiation or uncharged particle radiation (e.g., neutrons) can only lead to ionization indirectly because of the lack of charge. Since no work with neutrons was done during the course of this thesis, no detailed description of the interactions of neutrons with matter will be given in this thesis.

1.3 Interactions of photon radiation with matter

As already mentioned, electromagnetic radiation does not ionize directly but indirectly through the liberation of secondary electrons. In the interaction of photons with matter, a distinction is made between several physical processes. The probabilities of the different interaction modes are highly dependent on the energy of the incoming photons and the mass attenuation coefficient of the targeted material (Figure 1.2). [5] [8] [9] [10] [7]

- Elastic / Coherent Scattering: In this form of scattering, only the direction of movement of the incident photon is slightly altered, while the energy remains almost constant (in the mathematical description, the energy is assumed to be unchanged). When scattering at bound electrons one speaks of Rayleigh scattering, when scattering at quasi free electrons of Thomson scattering (borderline case of the Compton scattering for small

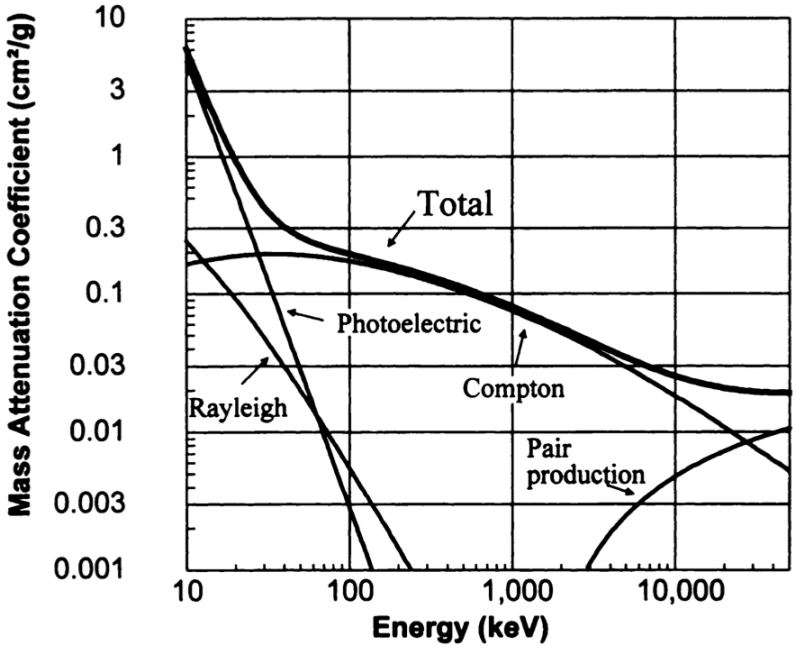

Figure 1.2: *Occurrence of the various interactions of photons with matter as a function of energy for soft tissue [7]*

photon energies). The elastic scattering at diagnostic energies (10-120 keV) has small to negligible probabilities of occurrence.

- Photoelectric effect: If an incident photon has enough energy, it can release an electron from an inner shell. The energy of the incident photon is split: the binding energy, which holds the electron, has to be overcome and the rest is transferred into kinetic energy of the now loose photo electron. The free electron position is filled by an electron of a higher shell, which in turn in turn leaves an empty position. It comes to an "electron cascade". By moving to a lower energy level either X-ray fluorescence radiation, which is characteristic for the element and the transition, or an Auger electron is emitted. Auger electrons represent a radiation less transition. Here the released energy is transferred to another electron in an outer shell, which thus has enough energy to leave the atomic shell. The photo effect is the predominant effect at photon energies up to about 25 keV in water (as well as in tissue), after which the Compton effect predominates (see next point).

A distinction must be made between the photoelectric effect and the nuclear photoelectric effect, in which photons are absorbed by the atomic nucleus and excite it. If the excitation energy is above a threshold energy for the emission of a nucleon, it comes to the release of one or more nuclear particles. The threshold energy depends on the nucleus and is between about 6 and 20 MeV. The most important reactions are (γ, n), $(\gamma, 2n)$ and (γ, p), which leave radioactive residues.

If the energy of a photon is insufficient to cause emission, the excited nucleus goes over to the ground state after the emission of a gamma quanta. This effect is called nuclear fluorescence.

- Compton effect: The Compton effect describes the interaction of a photon with a free or a valence electron. During the ionization of an atom described in this context, the photon energy normally exceeds the ionization threshold of the atom by a multiple. The photon is not completely absorbed, as it is for the photo effect, but is scattered and has thus a lower energy and a longer wavelength. The energy of the scattered photon depends on the energy of the incident photon and the photon scattering angle.

  The Compton effect is predominant in water (tissue) at photon energies from about 25 keV to 12 MeV.

- Pair production: An electron-positron pair can be formed in a strong Coulomb field, if the photon energy exceeds the energy-mass equivalent E_γ for two stationary electrons with mass m_e: $E_\gamma > 2m_e c^2$, with c being the speed of light. The photon is completely absorbed and the photon energy is partly used for the formation of the electron-positron pair (at least 1022 MeV) and partially converted into kinetic energy of the two particles.

  After the formation of the electron-positron pair, the electron is attracted to the nucleus and the positron is repelled. Both lose their energy through collisions in small portions. After the positron has come to rest, it recombines with an electron. As a result of this recombination, the rest mass of the two particles is usually converted into two photons each having an energy of 511 keV, which are emitted at 180 degree with respect to each other.

1.4 Interaction of charged particles with matter

The interaction probability of charged particles is almost guaranteed, as opposed to that of uncharged particles, due to their electric field. In general, one differentiates between [5] [10] [1] [11]:

- Interaction with orbital electrons: A particle, whose impact parameter is large enough, interacts with the entire atomic shell. On the one hand this can lead to a change of direction of the colliding particle and to a very small change of energy (corresponds to an elastic collision). On the other hand it can lead to an excitation or ionization of the collision partner, the so-called inelastic scattering.

  These two described phenomena can be summarized under the name ”soft collisions”. Particles slowed down via these interactions only loose a very small part of their energy per collision. It can be said that they are continuously slowed down. Soft collisions account for about 50% of the energy lost by charged particles. An incident particle can also interact directly with a single orbital electron and raise it to a higher energy state, or immediately lead to ionization. After both excitation, as well as ionization, the reoccupation of the electron hole leads to the emission of characteristic X-rays. This process is also known as ”hard collision” because the released electrons have a much higher energy than the electrons of the soft collisions and can in turn interact through soft collisions.

- Interaction with the Coulomb field of the atomic nucleus: With sufficiently high particle energy and a suitable low collision parameter, a particle can also interact directly with the Coulomb field of the atomic nucleus. This can lead to either elastic nuclear scattering, if the particle is scattered without loss of energy (very rare), or inelastic nuclear scattering. Here the particle is deflected with loss of energy in the Coulomb field and a part of the energy is converted into X-ray bremsstrahlung.

  The interaction with the Coulomb field of the atomic nucleus is predominant with electrons. Although it comes to deflections of protons and heavy ions due to interactions with the Coulomb field of the nucleus, the formation of bremsstrahlung is negligible.

- Reactions with the nucleus: With a very small impact parameter, the charged particle can also interact directly with the nucleus. Electrons interact only through the Coulomb

forces, while hadrons interact via the strong interaction and emission of nucleons can occur, as well as to the emission of gamma radiation.

However, these processes are very rare and therefore play a negligible role in the energy loss of charged particles.

Fundamental in connection with the interaction of charged particles in matter is the Bragg peak, which represents the maximum on the Bragg curve. This phenomenon is especially important in the dosimetry of proton/ion beams in radiotherapy. The Bragg curve describes the stopping power of charged particles in matter: the kinetic energy that particles lose along their path in the material. Protons/Ions are nearly continuously decelerated by Coulomb interactions with shell electrons. Due to their high mass, the direction of the protons changes only minimally. This phenomenon is often called multiple coulomb scattering (MCS). The linear energy loss S is described by the Bethe-Bloch equation:

$$S = \frac{\partial E}{\partial x} \propto \frac{1}{v^2} \cdot \frac{Z}{A} \cdot z^2 \tag{1.1}$$

where v is the velocity of the projectile, Z is the atomic number of the absorber, A is the mass number of the absorber and z is the charge of the projectile.

The linear energy loss corresponds to the average energy loss. In reality, the particles lose their energy in individual collisions. It should be noted here that the number of impacts is different for all particles. Therefore, they do not all come to a stop at the same point. The actual energy loss spreads around the mean. This is called range straggling.

Nuclear reactions with the nucleons play only a minor role during the stopping process, but must nevertheless be included. A consideration of all these phenomena results in the Bragg curve, which can be seen in Figure 1.1 and also includes the stopping power for photons and electrons as a comparison. It should be noted that electrons have no observable Bragg peak. They lose their energy compared to protons/ions by significantly more scattering processes, such as the generation of bremsstrahlung and thus come to rest in many different positions.

Looking at the dose deposition as a function of depth of photons or electrons (Figure 1.1), one notices that the maximum of the depth-dose curve is not located on the surface of the irradiated material (or tissue). It occurs only after a certain penetration depth. The reason for the so-called dose-building effect are forward scattered secondary electrons, which are

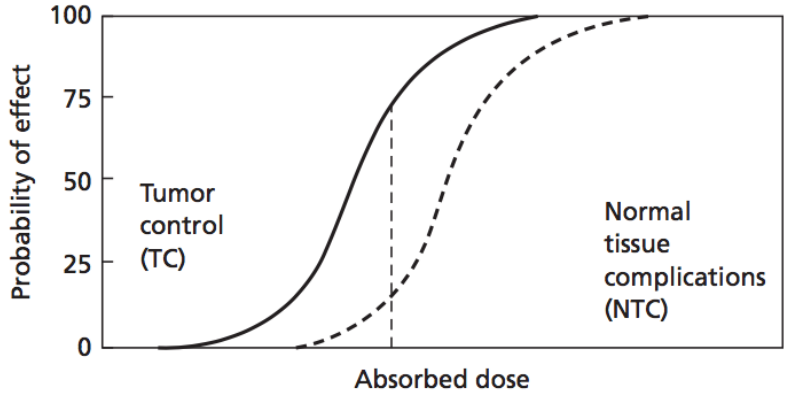

Figure 1.3: *Tumor control probability (TCP) and normal tissue complications (NTC) as a function of dose [1]*

released at the surface, but only transfer their energy deeper within the material. The build-up effect is always observed when the radiation traverses interfaces (e.g., air / tissue) and is more prominent at higher energy photon and electron radiation.

1.5 Interactions of ionizing radiation with biological tissue

Concerning the interaction of ionizing radiation with biological tissue, one distinguishes between direct and indirect radiation effects. Direct radiation damage occurs, when the radiation directly alters biomolecules in their structure (e.g., breaks up hydrogen bonds in the DNA) or forms radicals of this compound. Radicals are highly reactive atoms or molecules with at least one unpaired valence electron. Indirect radiation damage is caused by secondary chemical processes. Here, water molecules play the biggest role, since human cells consist of 80% water. Water molecules, as well as other structures of the cell plasma and those close to the DNA are altered and can interact with the DNA or other crucial biomolecules.

Permanent effects of ionizing radiation on living cells are highly dose dependent and the effects can be split into two types: stochastic and non-stochastic (deterministic).

- Stochastic effects are hypothesized to follow a linear, no-threshold model. This means, that although there is no threshold for adverse effects, the probability of them occur-

ring is highly dose dependent. Examples for stochastic radiation effects are the development of cancer, which can take a quite long latency of even a few decades.

- Deterministic effects on the other hand occur only if a certain dose threshold has been reached. The severity of these effects increase with increasing dose. The most common example of deterministic effects are skin burns.

Tumor tissue is more radio-sensitive compared to healthy tissue, therefore the threshold for deterministic damage is also lower in tumor cells. In healthy cells, cell-repairing mechanisms are much better and more targeted than in tumor cells. The aim of radiotherapy is to apply a high total dose to the tumor tissue and to spare the surrounding healthy tissue (Figure 1.3).

1.6 Generation of ionizing radiation

1.6.1 High energy X-rays and gamma radiation

As already mentioned in Section 1.4, the interaction of electrons with matter causes the emission of bremsstrahlung or characteristic X-rays.

A schematic representation of a X-ray tube is provided in Figure 1.4. An electron source in the form of a cathode (usually a hot cathode made of tungsten) is placed in an evacuated tube. Opposite is a positively charged anode, the target. Between the cathode and the anode is a high voltage, which accelerates the electrons to the anode. Upon impact with the target, X-rays are emitted which can escape through a window. Especially while producing high energy photons a cooling cycle is installed to avoid overheating of the anode. Outside the X-ray tube, collimator and filters are important. The filter is needed to remove low-energy X-ray radiation from the beam.

The energy of the X-rays depends on the applied voltage between anode and cathode. The maximum energy is equal to the maximum voltage along the X-ray tube (kVp, peak kilo voltage). The intensity of the X-radiation depends on the electron yield of the cathode.

The type of X-radiation described above is technically limited by the high voltage between the cathode and the anode, since one relies on the use of direct current. Fields over 500 keV can not be generated this way. For the higher energy range, devices such as linear accelerators or betatrons (obsolete) have been developed.

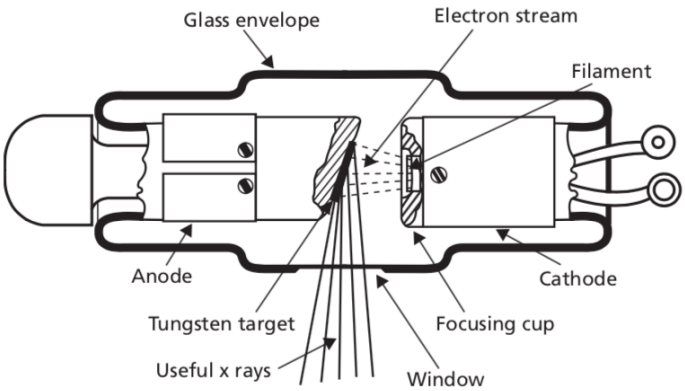

Figure 1.4: *Schematic overview of the setup of an X-ray tube [1]. X-ray tubes in this form are used for diagnostics as well as for therapeutic purposes up to around 500 kVp.*

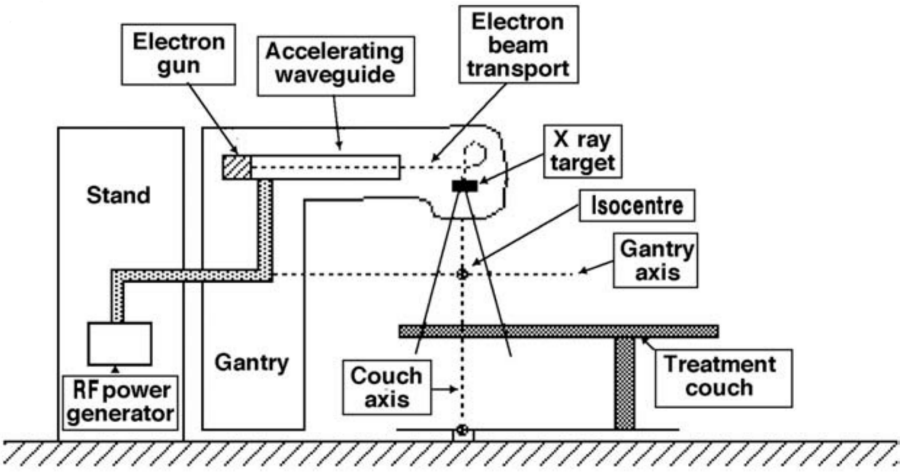

Figure 1.5: *Schematic overview of a linear accelerator [12]*

Medical linear accelerators (linac) are capable of producing electron or photon beams between 4 and 20 MeV, whereas energies up to 10 MeV are most practical to minimize activation and photon nuclear interactions. A schematic of a linac is shown in Figure 1.5. There are a few design choices concerning linacs. As only the one presented in Figure 1.5 is discussed here, the reader is referred to [12] for more detailed information.

The freeing of the electrons from a heated cathode as well as the initial acceleration with a electrostatic potential is identical to X-ray tubes. After this, the electrons enter the accelerating waveguide. The accelerating waveguide is a gas-filled or evacuated metallic structure and

used in the transmission of microwaves. The acceleration of the electrons is based on a power transfer from the high power radio frequency (RF) fields. The microwaves are generated by the RF power generating system. The waveguide is loaded with disks, which are used to slow the phase velocity of the RF wave down below the speed of light. the cavities between the disk serve to couple and distribute the RF power between the cavities and to provide a suitable electric field pattern for acceleration. Two types of accelerating waveguide are in use:

- Traveling wave acceleration: here the microwaves travels with the electrons. At the end of the waveguide the RF wave is either absorbed or fed back into the input end of the waveguide.
- Standing wave acceleration: here the wave is reflected at both the input and the exit of the waveguide. This results in the build up of a standing wave. Only every second cavity carries an electric field.

After further transport and bending of the electron beam the electrons strike the target, which is composed of a high Z material to maximize X-ray gain. Contrary to X-ray tubes, the target in linacs is hit in forward direction, as in the mega voltage range most photons are produced in the direction of the electron beam striking the target.

The X-ray beam is then shaped by special filters and collimators.

By removing the target electron beams can be created. As the pencil shaped Gaussian electron beams exiting the linac are not clinically useful, scattering foils, consisting of high Z material, are placed in the beam. After going through those foils, the beam has a broad spectrum. Again special collimators are placed to shape the beam.

The generation of high-energy gamma radiation is accomplished in telegamma machines with isotopes such as ^{60}Co or ^{137}Cs. ^{60}Co is used in medical areas as a calibration source, due to its long half life of 5.2714 years combined with the production of high intensity radiation. ^{60}Co is not a naturally occurring isotope, it is produced artificially in nuclear reactors by bombarding ^{59}Co with slow neutrons. The simplified β^- decay of ^{60}Co is depicted in Figure 1.6.

In Europe, these devices are no longer widely used for therapeutic procedures, as they have been replaced by linear accelerators. Linear accelerators have the advantage of not producing

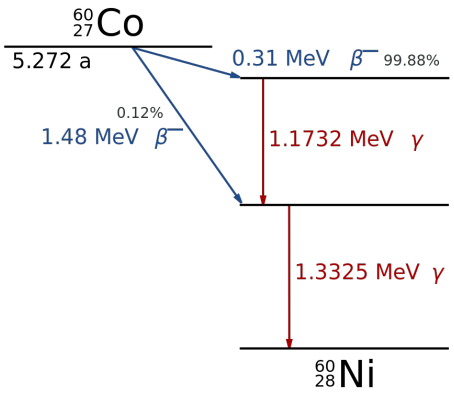

Figure 1.6: *Simplified decay schema of ^{60}Co to ^{60}Ni via β decay*

radioactive waste and generating radiation where the energy can be varied. For dosimetry on the other hand, ^{60}Co radiation is extremely important as dosimetric protocols define it as a reference radiation for the calibration of detectors.

1.6.2 High energy particle radiation

Cyclotrons and synchrotrons are used on the one hand to accelerate charged particles (with the exception of electrons, which can be better accelerated in linear accelerators), and on the other hand to generate radionuclides for therapeutic or diagnostic purposes. A cyclotron consists of two semicircular electrodes, which are arranged in a vacuum chamber between the poles of an electromagnet. An ion source is located between the electrodes. A charged particle is accelerated towards the electrode after exiting the ion source. In the electrode they are shielded from the electric field and the magnetic field brings the particles on a cyclic path. An alternating field applied to the electrodes deflects them in dependence on the strength of the static homogeneous magnetic field and the type of the particle in such a way that the particle always experiences an acceleration after exiting the electrode. The particles are emitted continuously and the particle beams have a fixed energy. The maximum velocity of the particles in a cyclotron (above all) is limited by its diameter (the larger the diameter, the greater the particle velocity), and by the strength of the magnetic field used.

In a synchrotron, in contrast to the cyclotron, the particle path is not spiral-like, but proceeds as a closed ring (with a fixed radius). Thus, the magnetic field can not remain constant in time, but must be increased in proportion to the increasing particle momentum. For accel-

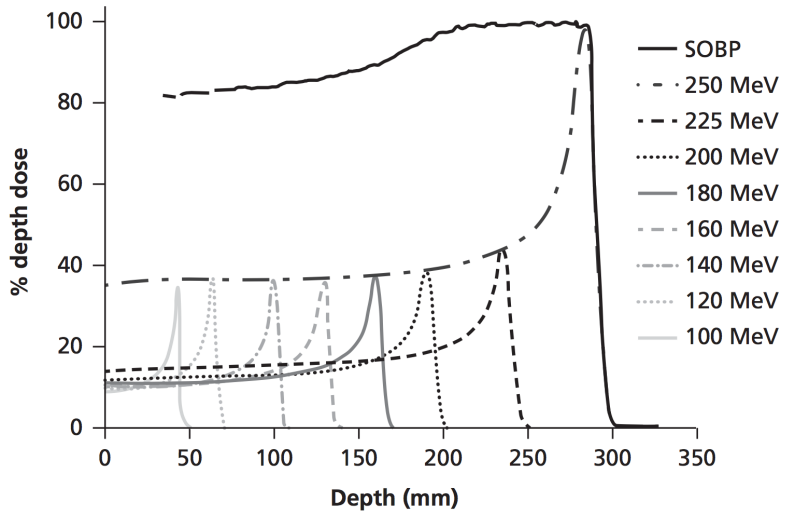

Figure 1.7: *Principle of generating a spread-out Bragg peak by addition of multiple beams with different energies [1]*

eration, high-frequency alternating electric fields are used. Inside the accelerator ring there is a high vacuum, so that the particles are not slowed down by collisions with gas molecules. In a synchrotron, the particles are emitted in packets and the beam energy can be varied more easily. In principle, higher particle energies are possible in a synchrotron than in a cyclotron.

1.6.3 Beam delivery systems in proton and light ion therapy

Currently there are three methods for beam delivery in proton and light ion therapy in use: passive scattering, uniform scanning and the active pencil beam scanning. [13] [14]

Passive scattering: The beam arriving in the treatment room has a single energy and usually a width of a few millimeters. The goal for passively scattered beams is it to deliver the dose over the whole planned target volume at once. Thus, the arriving beam needs to be spread out both in depth and laterally. Range modulation is achieved by placing absorbers, usually rotating range modulator wheels, in the beams path and thus achieving a stacking of Bragg curves with different energies (Figure 1.7). The widening of the beam to cover the lateral directions is achieved by placing scattering material in the path of the beam. Most commonly in use are double scattering systems (two scatterers) to achieve a uniform field

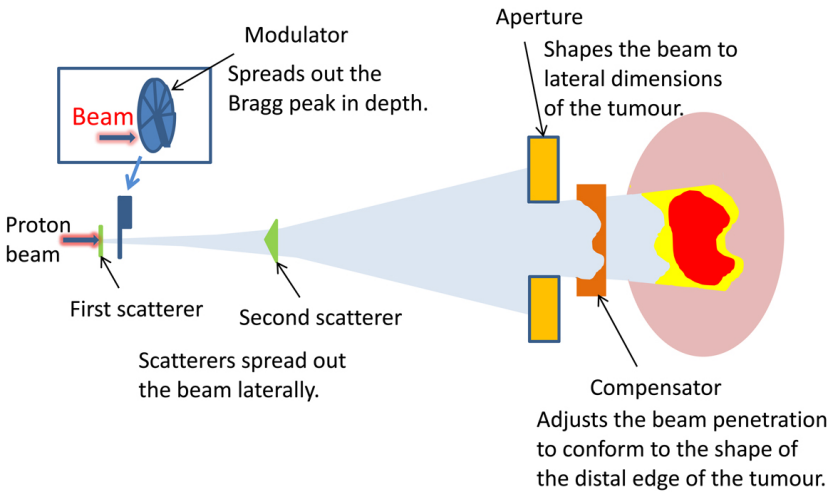

Figure 1.8: *Principle of the passive scattering method [14]*

distribution. Lastly, a collimator narrows the field again to the desired dimensions and a patient specific compensator is placed in the beam to conform the dose to the planned target volume. Figure 1.8 shows the principle arrangement of this method.

Uniform scanning: In contrast to the passive scattering method, the widening of the beam is here less pronounced, which means that only a single scatter is placed in the beam. The beam is only widened to a few centimeter and then the range modulated beam is scanned with the help of magnets over the whole lateral range of the planned target volume. Again, a patient specific compensator is placed int he beam. The arrangement can be seen in Figure 1.9.

Active pencil beam scanning: Here a single Gaussian-shaped pencil beam, or beamlet, is scanned with the help of magnets over the lateral region of the planned target volume. The slice-wise scanning is achieved by manipulating the beam energy, although no spread out Bragg peak is generated. Thus, every spot in the target volume is accessible and overranging is reduced to a minimum. A simplified arrangement can be seen in Figure 1.10.

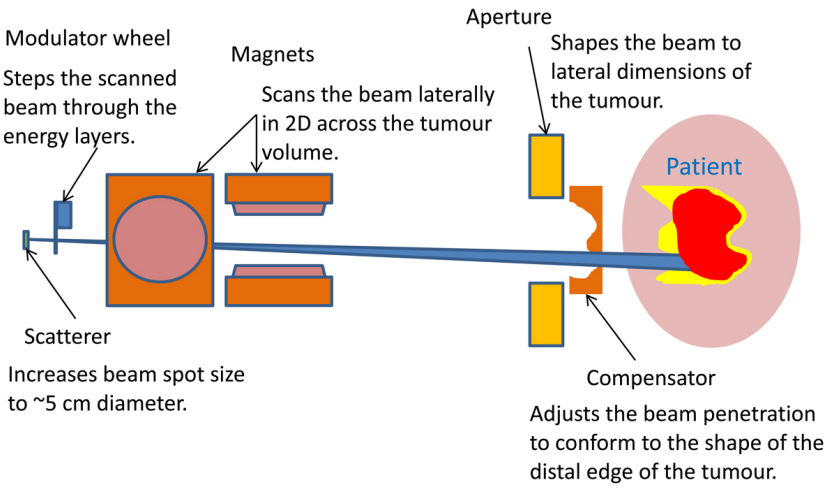

Figure 1.9: *Principle of the uniform scanning method [14]*

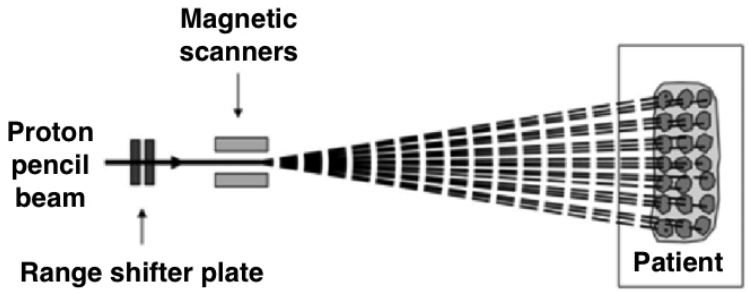

Figure 1.10: *Principle of the active pencil beam scanning method [15]*

1.6.4 MedAustron

MedAustron, the center for ion therapy and research (founded as EBG MedAustron in 2007), is a center for ion beam therapy and non-clinical research located in Wiener Neustadt, Austria. It is worldwide the 6th combined center for ion beam therapy with both protons and carbon ions. Carbon treatment is forseen to start in 2019. The centerpiece of the facility is the synchrotron with approximately 80 m in diameter. The ions are provided from 3 ion sources by heating either carbon dioxide or hydrogen gas to a plasma and separating the positively charged ions with the use of electric fields from the electrons. The ions are pre-accelerated in a linear accelerator before being injected into the synchrotron, where they are further accelerated until the desired energies are reached. Proton energies range from 62.4 MeV to 252.7 MeV clinically, while the synchrotron can reach higher energies (up to

800 MeV) for non-clinical research purposes. After acceleration the beam reaches the treatment room. There are four treatment rooms available at MedAustron, where three are used clinically. [16] [17]

1.7 Dosimetry

During irradiation of any material energy is transferred from the radiation field to the material. The measurement, calculation and assessment of the absorbed energy by the material due to irradiation is defined as radiation dosimetry. The most commonly identified physical quantity in dosimetry is the absorbed dose D, which is represented as the absorbed energy E per unit mass m of the material, with the unit $1J/kg = 1Gy$:

$$D = \frac{\partial E}{\partial m}. \tag{1.2}$$

In dosimetry in the medical field absorbed dose to water is most important, as the human body consists to approximately 80% of water. Thus, dosimeters are usually placed in water or, especially for those not watertight, in other water-equivalent solid materials.

There are a variety of dosimeters, specialized to certain application areas. Therefore, only the operation principles of dosimeters used during the course of this work, will be discussed.

1.7.1 Ionization chambers

Ionization chambers represent gas or liquid filled detectors, which measure ionizing radiation by collecting the produced secondary charges in its volume. This results in both a signal for the number of collected ions and the rate of their collection. Most ionization chamber consist of a gas filled cavity and two electrodes, used to create an electric field in the gas. The shape of the electrodes depend on the type of ionization chamber used. The ionization chambers used here are vented, thus operate under atmospheric pressure, and watertight.

Irradiation of an ionization chamber leads to the creation of ions inside the gas filled volume. In the applied field, the newly formed cations and electrons move to the electrode of opposite polarity, where they are collected. The electric field has to be strong enough to pre-

vent ion recombination before reaching the collecting electrode. The continuous collection represents an ionization current, whose measurement is performed by an electrometer.

The calibration of dosimeters, including ionization chambers, is usually done in reference radiation (^{60}Co radiation) and afterwards the reading of the electrometer is modified via correction factors to the used beam quality and type (k_{Q,Q_0}). This applies also for irradiation with protons, no standard laboratory offers calbration in proton beams.

Further corrections include any aberrations from reference conditions, where the most common is the temperature and pressure correction k_{TP}. The response of an ionization chamber differs for measurements performed with temperature (T) and pressure (P) different from standard reference temperature ($T_0 = 20°C$) and pressure ($P_0 = 1013hPa$). The correction factor k_{TP} is defined as [18]:

$$k_{TP} = \frac{273.3 + T}{273.2 + T_0} \cdot \frac{P_0}{P} \tag{1.3}$$

Further correction factors include, but are not limited to:[18]:

- k_{Q,Q_0}: corrects for differences in user beam quality compared to reference beam quality
- k_{TP}: corrects for temperature and pressure variation from reference conditions
- k_{elec}: is needed if the ionization chamber and the electrometer were calibrated separately
- k_{pol}: corrects for any differences in readings gathered at different applied chamber voltages
- k_S: represents a factor, which is applied to incorporate ion recombination and thus incomplete charge collection

Applying all correction factors lead to the absorbed dose to water $D_{w,Q}$:

$$D_{w,Q} = M_Q N_{D,w,Q_0} k_{Q,Q_0} \prod k_i \tag{1.4}$$

where M_Q is the reading of the electrometer, N_{D,w,Q_0} is the calibration factor in terms of absorbed dose to water in a reference beam and k_i represents all applied correction factors.

1.8 Dosimetry of small fields

The importance of small fields and subsequently consistent dosimetry of such fields has gained increasing importance, as already mentioned in section 1.1. A radiation field is characterized as small, if one or more of the following physical conditions applies [2] [3] [4] [19] [20].

- Lateral charged particle equilibrium (LCPE) along the beam axis is lost: This would lead in conventional dosimetry to a dose underestimation as a non-negligible part of the dose is delivered by secondary charged particles. In principle, LCPE is lost, if the beam half width or radius is smaller than the range of the lateral charged particles.
- The radiation source is partially shielded by collimators as viewed from the point of measurement: The shielding produces overlapping penumbras and an apparent widening of the field. Both those effects are explained graphically in Figure 1.11. The overlapping penumbras and the widening of the field result in a non-uniform dose distribution on the detector, which causes again a dose underestimation, due to the volume averaging effect. The volume averaging effect describes the differences in dose readings between a ideal, theoretical, infinitesimal small detector and the used real detector.
- The detector dimensions are similar or large in comparison with the field size: This can lead to challenges while aligning the detector with the field, as current codes of practice still recommend the use of very small dosimeters, like p-types or diamond detectors.

The loss of LCPE and the non-uniform dose distribution due to source occlusion is in practice unavoidable while using field sizes smaller than 3 cm $\times$ 3 cm [21]. It is clearly seen, that the need for consistent reference dosimetry and overcoming most, if not all, of these challenges is high.

1.9 The dose area product

To overcome the aforementioned challenges, an approach has been introduced using a detector many times larger than the field size. Usually a large area ionization chamber (LAIC) is

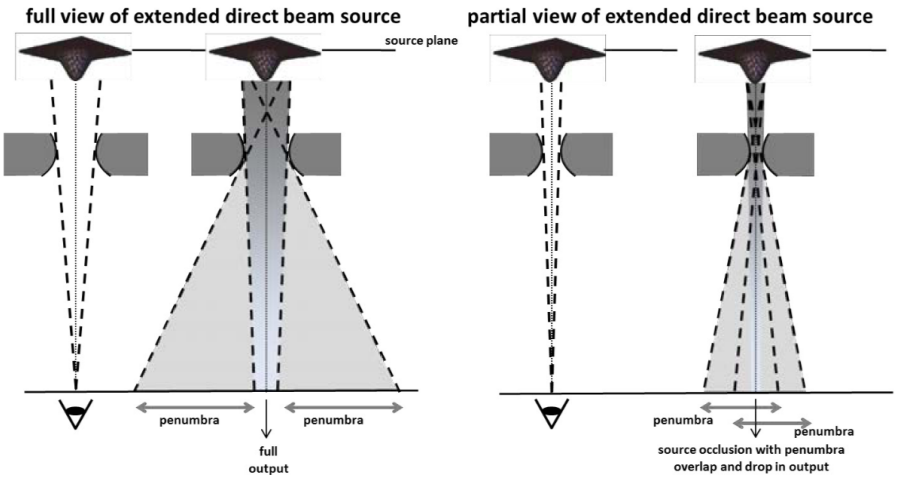

(a) *Schematic representation of the overlapping penumbras resulting form partial source occlusion [2]*

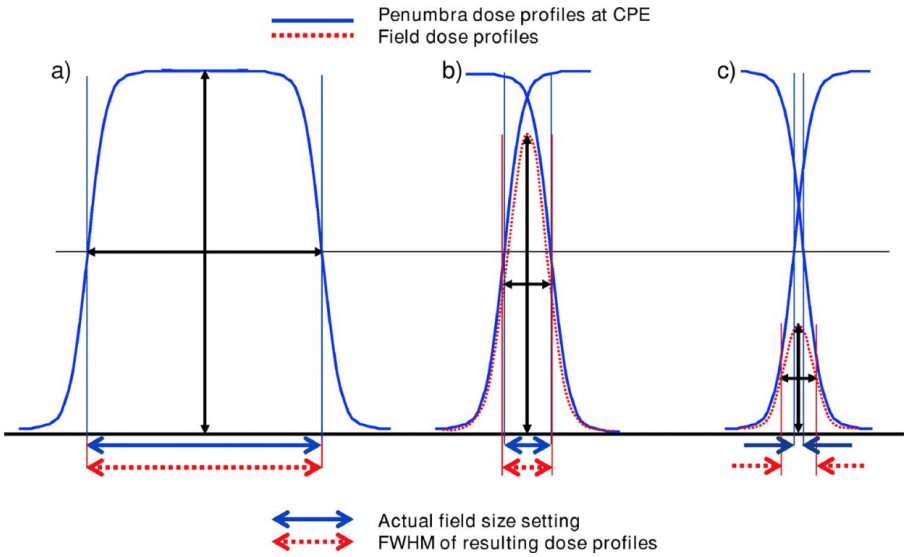

(b) *The overlapping penumbras have an effect on the FWHM of the beam. It is here illustrated for a big field, where the effect is negligible (a), whereas in (b) it causes a small error in field size estimation from FWHM. Finally in (c) the maximum of the field dose profile is pushed down and the FWHM is much larger than the actual field size [2] [21].*

Figure 1.11: *Graphic explanation of the creating of overlapping penumbras as well as the widening of the field due to partial source occlusion*

used to determine the dose area product (DAP) [20]. Positioning and volume averaging effects are omitted when using LAICs, due to their large active area, as well as non-uniformity issues of the beam, since LAICs integrate the dose. The deposited energy over the whole sensitive area of a detector perpendicular to the beam direction represents the DAP, with its unit $Gy \cdot cm^2$ [19]. With a known dose distribution over a 2-dimensional area, measurements of the DAP allow the dose output perpendicular to the beam to be identified. The DAP is especially useful in scanned proton beams, as it represents the dosimetric equivalent of the incident number of particles on the detector.

Most commonly the DAP in water (DAP_w) at a certain depth (z) in scanned proton beams is calculated via [22]:

$$DAP_w(z) = MN_{DAP,w,Q_{cross}} \Delta x \Delta y k_{Q,Q_{cross}} \cdot \prod k_i \tag{1.5}$$

where M corresponds to the reading of the detector and $N_{DAP,w,Q_{cross}}$ to the calibration factor of the LAIC in respect to absorbed dose to water. $k_{Q,Q_{cross}}$ represents the beam quality correction factor and k_i all other applied correction factors (section 1.7.1). Q_{cross} is used instead of the usual reference quality Q_0, as no current standard laboratory provides calibration in terms of absorbed dose to water, thus a cross calibration is unavoidable.

2 Materials

2.1 X-ray unit

Figure 2.1: *X-ray unit: Yxlon Maxishot*

The X-ray unit utilized in this work is of type Yxlon Maxishot (YXLON International GmbH, Hamburg, Germany) [23] (Figure 2.1). It is an oil cooled, commercially available unit. The X-ray tube (type: Y.TU 320-D03) is mounted on the right hand side of the steel container to provide a horizontal beam. This design was chosen to provide a reference beam for comparison with the horizontal proton beam in the research irradiation room (IR1) at MedAustron. The steel container additionally provides lead shielding. Its dimensions are 1889 mm $\times$ 928 mm $\times$ 1384 mm (L $\times$ W $\times$ H). The acceleration voltage of the tube can be varied between 10 kV and 200 kV. The maximum current is 21 mA. The anodes target

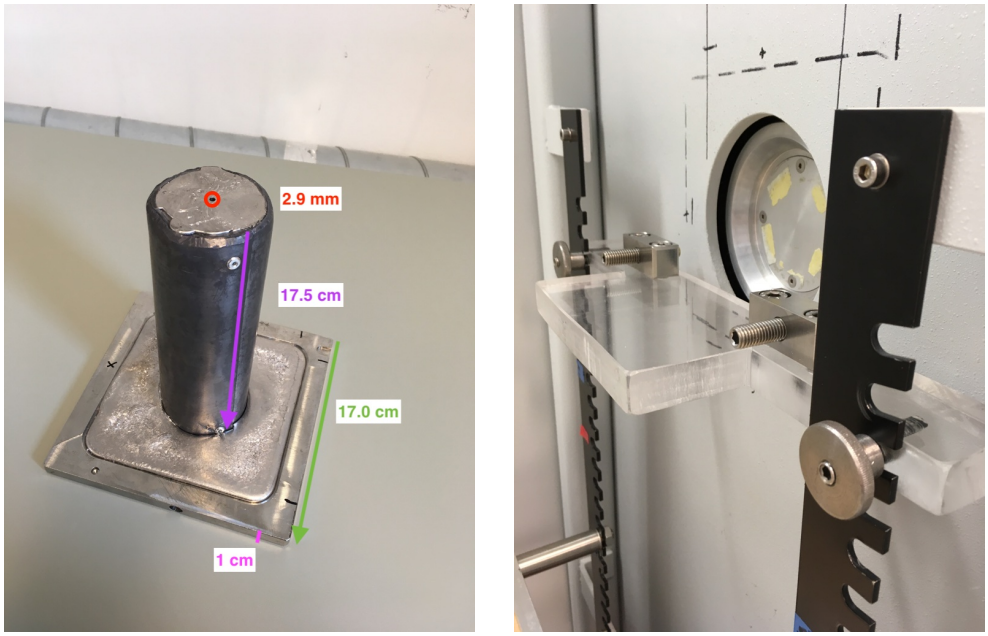

(a) *The in-house built collimator has following dimensions: quadratic end-plate side length (green) = 17 cm, end-plate thickness (pink)= 1cm, length (purple) = 17.5 cm, and opening hole diameter (red) = 2.9 mm*

(b) *Holder to mount the collimator in front of the beam exit window*

Figure 2.2: *The collimator with its holder used to create a collimated X-ray beam*

material is tungsten, with a flat target type and a target angle of 20°. The focus size can be switched between 3.0 mm and 5.5 mm. The pre-filtration of the beam is threefold: 3.0 mm Beryllium, 3.0 mm Aluminum, and 0.5 mm Copper.

An outside control unit is used to set the irradiation parameters, i.e. acceleration voltage, current, focus size, and irradiation time. The irradiation time can be set in a minimum of 1 second intervals and can also be set to indefinite with a manual stop.

The measurements were performed with an in-house designed lead collimator to create a collimated X-ray beam (see Figure 2.2). It has a quadratic end-plate of approximately 17 cm $\times$ 17 cm. The beam exit opening (marked with red circle in Figure 2.2a) has a diameter of 2.9 mm. The collimator can be attached directly in front of the beam exit window.

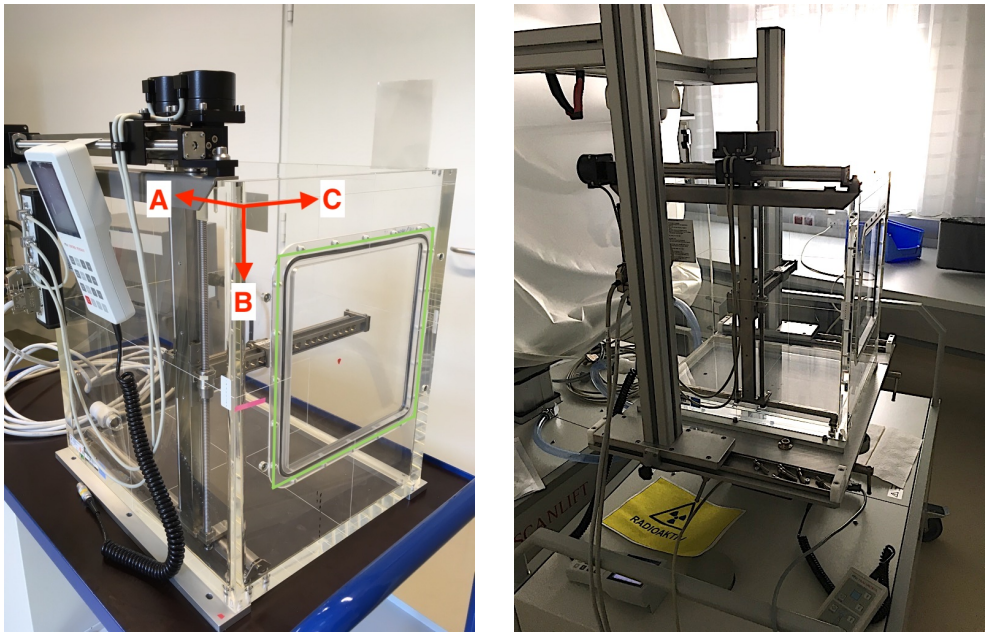

(a) *The water phantom removed from the reservoir: red arrows mark the movement axes and the green rectangle surrounds the entrance window*

(b) *The water phantom attached to the water reservoir*

Figure 2.3: *Water phantom MP3-P (PWT)*

2.2 ^{60}Co source

The ^{60}Co unit used for the cross calibration of the BPC150 is a radiotherapy unit of type Theratron 780C, which is located at AKH Wien / MedUni Wien. The field size can be adjusted manually directly at the machine, while the irradiation time is set via a control unit outside the irradiation room.

The last absolute dosimetry investigation with this unit was performed on June 16th 2016 with the Farmer chamber where a dose rate of $0.215\ \frac{Gy}{min}$ was determined for a 10 cm $\times$ 10 cm field at 10 cm depth RW3 (standard reference conditions following international recommendations).

2.3 Water phantom

In general water equivalent materials, such as special plastic phantoms or solid water, are used for dosimetric examinations. [5] [10]

During this work, the MP3-P and the MP3-PL Phantom tank from PTW (PTW Freiburg GmBH, Freiburg, Germany) [24] [25] were used, which were designed for dosimetry in photon and particle beams. Only the smaller phantom (MP3-P) fitted into the Yxlon unit.

During measurements with protons the MP3-PL water tank was used. A selection of the most important technical specifications for both water tanks can be seen in Table 2.1.

The water phantoms consist of a PMMA tank, a moving mechanism and a control unit. The entrance window (marked with green rectangle for the MP3-P in Figure 2.3a) allows measurements with a horizontal beam. The entrance window is thinner compared to the wall thickness of the overall phantom. The movement mechanism consists of 3 separately addressable arms, which move along the A-, B-, and C-axis (see Figure 2.3a) with a step interval of 0.1 mm and a positioning accuracy of 0.5 mm. The position can either be adjusted via a control pendant or remotely with a computer while using the MEPHYSTO software. The MP3-P water phantom with its corresponding movement axes can be seen in Figure 2.3a.

The tank is mounted on a water reservoir (see Figure 2.3b) and the water can be directly pumped inside.

During measurements inside the Yxlon X-ray unit the tank was dismounted from the reservoir as the measurements were performed in air. The entrance window was removed while conducting the measurements with the collimator as it was obstructive for both the transmission monitor chamber and its holding mechanism and without the entrance window a closer overall detector-collimator distance could be achieved.

Table 2.1: *Selection of technical specifications for the MP3-P and the MP3-PL water tank according to PTW manual [24] [25]*

	MP3-P	MP3-PL
Ouside dimensions [mm]	$484 \times 498 \times 386$	$630 \times 520.5 \times 632$
Moving range [mm]	$350 \times 380 \times 250$	$500 \times 408.5 \times 500$
Wall thickness [mm]	18	18
Entrance window dimensions [mm]	$250 \times 250 \times 0.5$	$250 \times 250 \times 0.5$
WET of entrance window [mm]	5.84 ± 0.01	5.85 ± 0.01
Filling capacity [l]	72	170
Step interval [mm]	0.1	0.1
Position accuracy [mm]	0.5	0.5

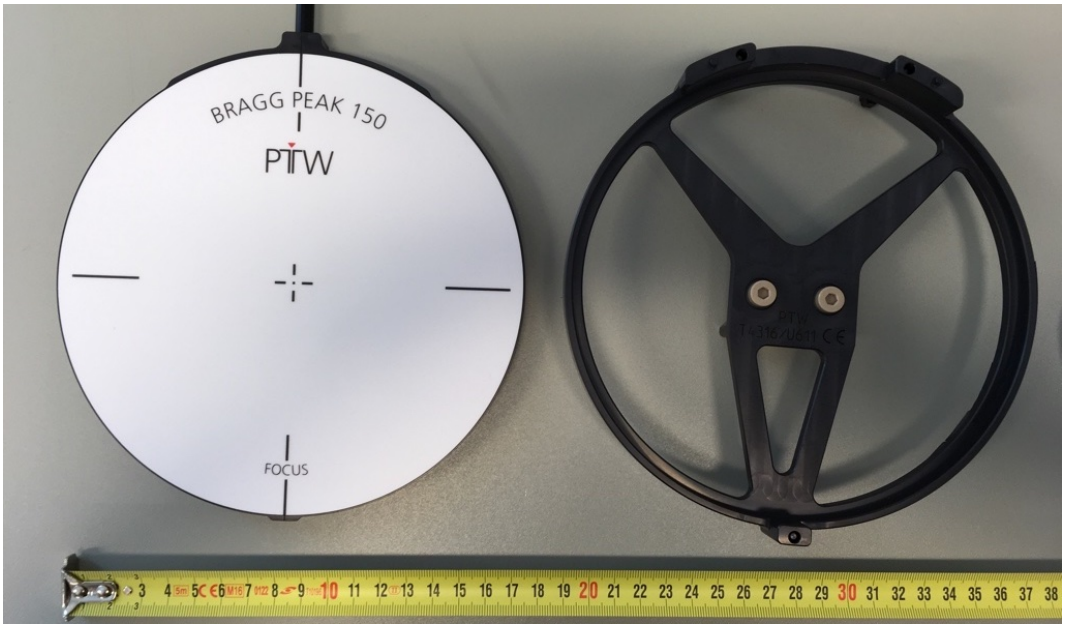

Figure 2.4: *Left: Bragg Peak Chamber under investigation (BPC150); Right: its custom made holder*

2.4 Ionization chambers

A Bragg Peak Chamber (serial number: 151058) with a diameter of 175 mm from PTW (PTW Freiburg GmBH, Freiburg, Germany) was thoroughly investigated in this MSc project. The manufacturer specifies a circular active diameter of 147 mm, thus the chamber will be further referred to as BPC150. The entrance window thickness is 2.89 mm, consisting in detail of 0.29 mm polycarbonate foil, 0.1 mm glass reinforced plastic, 2.47 mm carbon fiber

Table 2.2: *Overview of the used LAICs and selected technical specifications, which were gathered from the corresponding manuals: [26] [27]*

	BPC150	PTW34070	PTW34080	PTW34073	Roos
Serial number	151058	118, 124, 125	–	031	2460
Diameter [mm]	175	103.95 ± 0.15	103.95 ± 0.15	67.95 ± 0.15	43.95 ± 0.15
Active diameter [mm]	147	81.6 ± 0.2	81.6 ± 0.2	39,6 ± 0.2	23.8± 0.15
Measurement volume [cm^3]	25.5 [1]	10.5	10.5	2.5	0.35
$WET_{entrance}$ [mm]	4.63 [2]	4	0.7	1.3	1.3
Nominal voltage [V]	400	400	400	400	200

[1] This value represents a crude approximation with a high uncertainty
[2] Will be discussed in Chapter 3.3 and Chapter 4.2

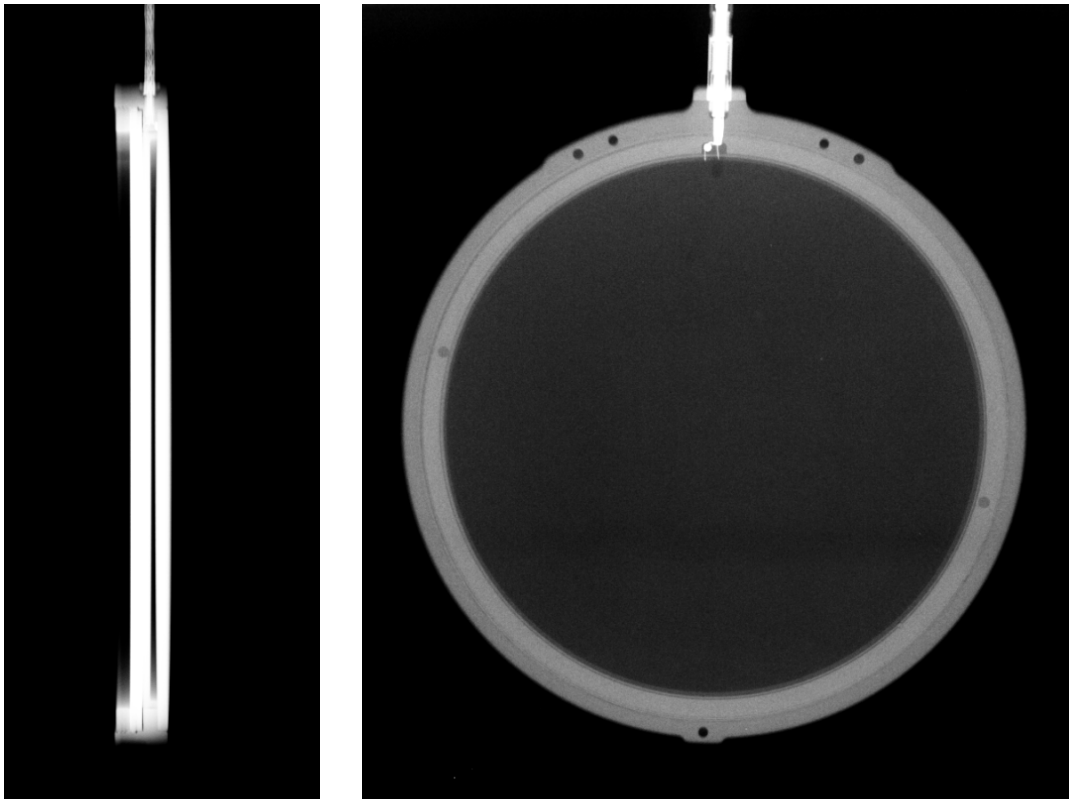

(a) *X-ray of the BPC150 in lateral direction. The gap represents the active volume.*

(b) *X-ray of the BPC150 in top-view*

Figure 2.5: *X-ray images of the BPC150 to asses for internal damage. Those images represent an average over 5 frames taken at 60 kVp with 20 mA for a duration of 10 ms.*

reinforced plastic and 0.03 mm graphite. The water equivalent thickness of the entrance window ($WET_{entrance}$) is not yet specified by the vendor, but was measured during the scope of this work. The nominal applied chamber voltage lies at +400 V, which was used for all measurements. Figure 2.4 depicts the BPC150 along with its custom made holder. During the scope of this work X-ray images of the BPC150 were taken, which are shown in Figure 2.5. As can be seen nicely, the gap in Figure 2.5a, which represents the active volume, is very regular and its edges are straight, therefore it can be assumed there is no visual damage of the chamber. Those X-ray images were also taken as a base to estimate the measuring volume, as this technical specification (among others, e.g the water equivalent thickness) was not yet

specified by the vendor. Using the X-ray images the size of the gap was compared to the known dimension of its diameter. This crude appraisal resulted in a measuring volume of 25.5 cm^2. It is emphasized again that it is a very rough estimate with a high uncertainty.

The measurement results obtained with the LAIC PTW34070 serves as benchmark to those of the BPC150. The PTW34070 has a diameter of 103.95 $\pm$ 0.15 mm and an active diameter of 81.6 $\pm$ 0.2 mm. The entrance window corresponds to a water equivalent thickness of 4 mm and the nominal voltage applied amounts to +400 V. [26]

As transmission monitor chamber the PTW34080 was used. It has an active diameter of 103.95 $\pm$ 0.15 mm and an active diameter of 81.6 $\pm$ 0.2 mm. The entrance window corresponds to a water equivalent thickness of 0.7 mm and the nominal voltage applied amounts to +400 V. [26]

During measurements with carbon ions the PTW34073 was used. It has an active diameter of 67.95 $\pm$ 0.15 mm and an active diameter of 39.6 $\pm$ 0.2 mm. The entrance window corresponds to a water equivalent thickness of 1.3 mm and the nominal voltage applied amounts to +400 V. [26]

For all above mentioned chamber types, with the exception of the BPC150, the manufacturer stated that no pre-irradiation is required. However one was performed before all measurements for all chambers.

The Roos chamber was used during the cross calibration in proton beams. It has a diameter of 43.95 $\pm$ 0.15 mm and an active diameter of 15.6 mm. The entrance window corresponds to a water equivalent thickness of 1.3 mm and the nominal voltage applied is +200 V. According to the manufacturer a pre-irradiation of at least 1 Gy has to be applied. [27]

All above mentioned LAICs are vented, watertight and suitable for dose and dose rate measurements in radiation therapy.

Table 2.2 gives an overview for all used LAICs and their mentioned technical specifications and Figure 2.6 provides a comparison of the diameters and active diameters.

During the cross calibration with ^{60}Co radiation a cylindrical Farmer type ionization chamber of type 30013 (PTW Freiburg GmBH, Freiburg, Germany) was used as reference detector [28]. It is a vented shell chamber used for absolute and relative dosimetry in high energy photon, electron and proton beams. It has a nominal sensitive volume of 0.6 cm^3 and requires no pre-irradiation. The schematics of the Farmer type chamber can be seen in Figure 2.7.

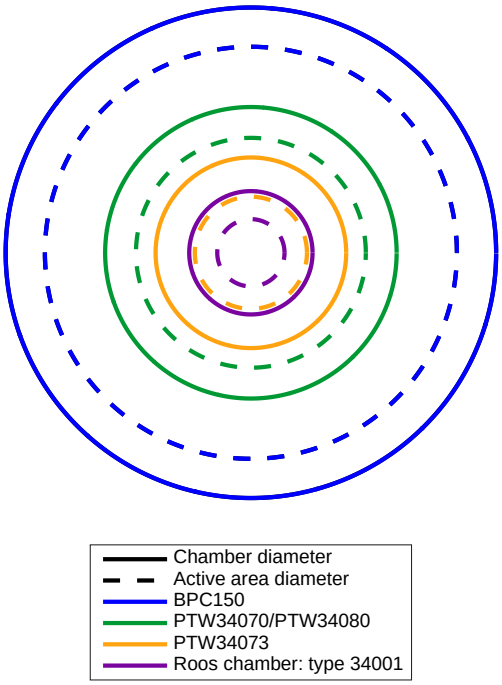

Figure 2.6: *Visual comparison of the diameters and active diameters of the LAICs used. Solid lines refer to the chamber' diameter and dashed lines to the diameter of the active area of the chambers.*

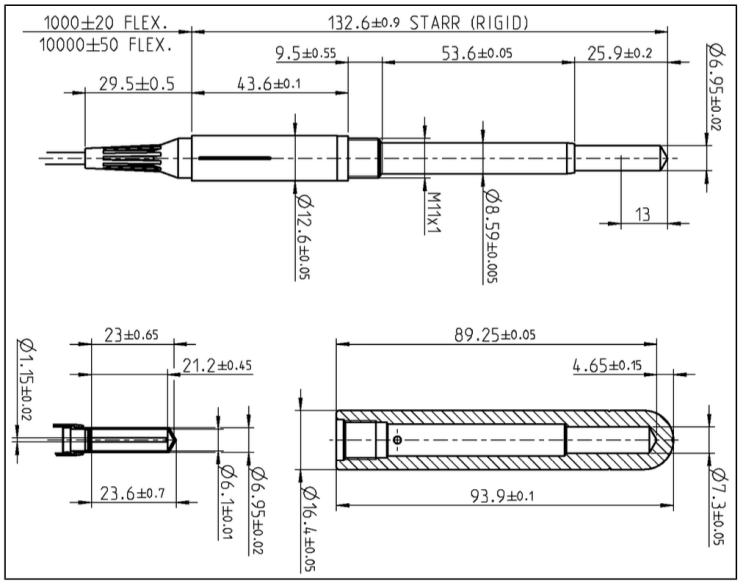

Figure 2.7: *Specifications for the cylindrical farmer type ionization chamber used during the cross calibration of the BPC150 in ^{60}Co radiation [28]*

2.5 Electrometer and software

A PTW Unidos webline electrometer (serial number 883) was used for the calibration in ^{60}Co radiation and the DAP measurements [29]. Measured dose and dose rate units can be either given as radiological units, provided the detector has been adequately calibrated, or in the electrical units charge (C) and current (A). The detector voltage can be varied between -400 V and 400 V in 1 V steps.

During the measurements in the Yxlon X-ray source a TANDEM XDR (PTW Feiburg GmBH, Freiburg, Germany) was used [30]. It is a dose rate measuring device with two channels for both a field and a transmission monitor chamber. It was connected to a TBA CONTROL UNIT (PTW Freiburg GmBH, Freiburg, Germany) [31] to manage the movement of the chamber inside the water tank remotely controlled by the software MEPHYSTO (**Me**dical **phys**ics **to**ol, PTW, Freiburg GmBH, Freiburg, Germany). MEPHYSTO is used for automatic acquisition and evaluation of relative and absolute dose measurements. This allowed the recording of two dimensional dose response maps.

2.6 Peakfinder

In order to assess the water-equivalent thickness (further WET) of the whole BPC150 the PEAKFINDER (PKF) water column (PTW Feiburg GmBH, Freiburg, Germany) was used. It is a high precision tool to measure intensity depth dose (IDD) curves in proton, as well as heavy ion beams and is specifically designed for 1-dimensional dose scans. Between two sealed bellows a thin windowed measurement ionization chamber (PTW34080) is placed in air. While moving the measurement chamber, the thickness of the water layer between entrance window and measurement chamber changes accordingly. The position accuracy of the PKF is 100 μm. A transmission monitor chamber (PWT34082) is fixed 12 cm behind the PKF front surface. The electrometer used during measurements with the PKF was the TANDEM XDR. The applied chamber voltage was +400 V. [32]

2.7 Particle irradiation at MedAustron

MedAustron is a synchrotron based facility that provides scanned proton and carbon beams. The facility is based on the PIMMS (proton ion medical machine study) design and can

accelerate protons and carbon ions to therapeutic energies and beyond. The particles are extracted from the accelerator in spills, with the minimum being $1 \cdot 10^{10}$ particles for protons and $4 \cdot 10^{8}$ particles for carbon ions. The nominel spill lenght is 5 seconds with a spill pause of 2 seconds. A spill abortion was recently implemented, which makes it possible to reduce the spill lenght depending on the reqiured particle number. It is possible to either irradiate a single spot, with spot sizes ranging from $4 - 10$ mm FWHM in vacuum depending on the energy, or to irradiate a whole field by scanning the particle beam over the whole area. The field size is limited to 20×20 cm^2. Using a beam degrader it is possible to attenuate the beams intensity to the specified need using filters. The transparency of the filter is given in the following manner: degrader 100 means no filter is in place, thus no particles are attenuated; degrader 20 means 20% of the beam is unattenuated. There are four degrader settings available: 10%, 20%, 50% and 100%. [33]

During medical treatment a complex 3 dimensional dose distribution is needed to irradiate each spot of the tumor adequately. Thus, a different number of particles with varying energy is needed, which is achieved with the help of the dose delivery system (DDS). The DDS is responsible for delivering the dose according the the afore defined properties. This is done with the use of integrated ionization chambers for measuring the absorbed dose per particle and an active feedback loop measuring for the disruption of the beam after the dose limit is met. [34] [35]

3 Methods

3.1 Temperature and Pressure correction

The reading of the electrometer M was gathered in electrical units. The reading of the ionization chamber was corrected (M_{corr}) for temperature and pressure variations from the standard reference during the measurements. The correction factor k_{TP} is defined in Equation 1.3.

$$M_{corr} = k_{TP} \cdot M \tag{3.1}$$

During measurements with the Yxlon X-ray unit, temperature (in $^{\circ}C$) and pressure (in hPa) were measured inside the steel container. A real time surveillance of the thermometer and barometer was not possible, as the door of the X-ray unit cannot be opened during irradiation and there was no integrated video signal or similar technique. Thus, temperature and pressure were recorded at the beginning and the end of each measurement and a linear relationship was assumed as an approximation. The interpolated values were then used to calculate k_{TP} .

During the cross calibration in a ^{60}Co beam also no real time surveillance of T and P was possible. Both values were checked before and after each measurement. However, due the good ventilation in the room where the Theratron 780C radiotherapy unit was located, combined with the relatively short measurement times, the changes in T and P were negligible.

In the proton irradiation room (IR1) temperature and pressure could be checked in real time with video surveillance of the thermometer and barometer.

3.2 Cross calibration in ^{60}Co radiation

Chapter 1.7 and especially Equation 1.4 describe the basics for dosimetry in water and water equivalent materials. For ^{60}Co radiation Equation 1.4 reduces to:

(a) *The setup for calibration of the Farmer Chamber*

(b) *The setup for calibration of the BPC150*

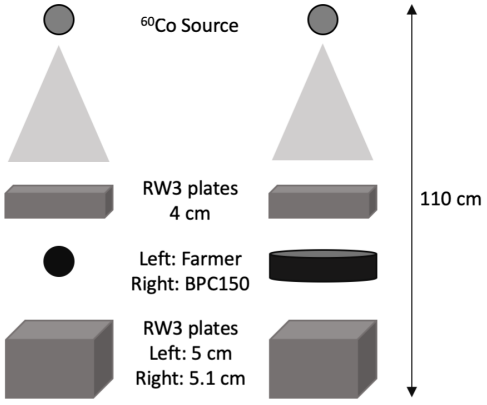

(c) *Schematic setup during the measurements with ^{60}Co radiation to achieve identical distances and attenuation for both chamber types*

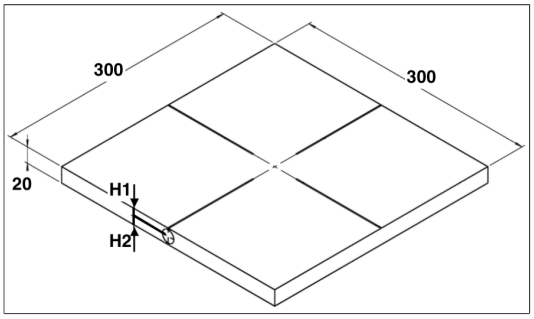

(d) *Schematics for the RW3 slab phantom for the Farmer chamber; the distances H1 = 7 mm and H2 = 13 mm are measured form the top/bottom of the RW3 slab phantom to the chamber center[36]*

Figure 3.1: *Experimental setup in the ^{60}Co source Theratron 780C radiotherapy unit at AKH Wien / MedUni Wien are presented in (a) and (b) and a schematic representation can be seen in (c); (d) provides an overview of the RW3 slab phantom*

$$D_w = MN_{D,w} \prod k_i \tag{3.2}$$

with M being the reading of the electrometer, $N_{D,w}$ is the calibration factor and k_i represents all applied correction factors (as outlined in Chapter 1.7.1) [18]. As ^{60}Co radiation is defined as reference radiation, the factor k_Q reduced to 1.

To determine $N_{D,w}$ of an uncalibrated chamber (BPC150) a cross calibration against a chamber with known $N_{D,w}$ (calibrated in a standard laboratory), which in this study was a Farmer type chamber, can be performed. The calibration factor of the Farmer type chamber in terms of absorbed dose to water was $N_{D,w} = 5.37 \cdot 10^{-2} \frac{Gy}{nC}$, as provided by Seibersdorf Laboratories on June 16$^{\text{th}}$ 2016.

For adequate cross calibration both chambers were placed successively in the radiation field at the same reference depth ($z_{ref} = 4\ cm$ RW3), beginning with the chamber with the known calibration factor. After the irradiation of the chamber with the unknown calibration factor the first chamber was irradiated again. This was done in order to rule out and/or detect changes during the calibration procedure, as the measurement data should not vary substantially from the first irradiatiion.The chambers were irradiated for the same amount of time. The electrometer readings were recorded and afterwards the k_{TP} factor was applied. Thus, M_{Farmer} (i.e. reading obtained with the Farmer type chamber) and M_{BPC150} (i.e. the reading obtained with the BPC150) represent the already k_{TP} corrected readings for the corresponing chamber in Equation 3.3. As the dose administered to both chambers was the same and no further corrections were needed, the calibration factor for the BPC150 ($N^{BPC150}_{D,w,cross}$) was calculated via rearranging Equation 3.2 [18]:

$$N^{BPC150}_{D,w,cross} = \frac{M_{Farmer}}{M_{BPC150}} N^{Farmer}_{D,w} \tag{3.3}$$

Experimental setup: For the setup of the Farmer chamber cross calibration RW3 plates were stacked on the bottom of the machine to a height of 5 cm . Then a RW3 slab phantom, designed to position the Farmer chamber inside was placed on top. Additionally, 4 cm of RW3 were placed above this holder. The setup can be seen in Figure 3.1a. Figure 3.1d provides a schematic representation of the dimensions of the Farmer-RW3 slab phantom.

The BPC150 chamber was placed on 5.1 cm RW3 plates to guarentee the same geometry during cross calibration. The additional 1 mm arises from the different chamber dimensions, as well as from the RW3 slab phantom for the Farmer chamber [36]. The reference point of the Farmer chamber is on the central axis at the centre of the cavity volume [18], which corresponds to:

$$50\ mm(RW3\ plates) + 13\ mm(RW3\ slab\ phantom) = 63\ mm$$

The reference point of plane-parallel chambers is on the inner surface of the entrance window. The BPC150 thus had its reference point at

$$50\ mm(RW3\ plates) + 15\ mm(total\ chamber\ height) - 3\ mm(entrance\ window) = 62\ mm$$

Thus, the additional 1 mm of RW3 was necessary to assure the same measurement depth. 4 cm of RW3 were set on top. The setup for the BPC150 can be seen in Figure 3.1b. Figure 3.1c provides a schematic overview of both experimental setups.

The cross calibration was performed with an irradiation time of 5 minutes and a 19 cm $\times$ 19 cm field. For the first and second step the measurements were repeated 5 times, while for the third step only 2 repetitions were performed, as no differences were observed. The dose in this period was 0.61 Gy.

3.3 Assessment of the water equivalent thickness

The WET for the BPC150 was assessed twofold:

- WET of the whole chamber
- WET of the entrance window.

WET of the whole chamber (WET_{total}^{BPC150}): This factor was determined by range measurements using the PKF in a proton beam. Figure 3.2a depicts the experimental setup in the research irradiation room (IR1) at MedAustron. The entrance window of the PKF was aligned with the IR1 isocenter using the room's laser guide system. First, 3 reference range measurements were performed with the PKF at a beam energy of 97.4 MeV. Then, the

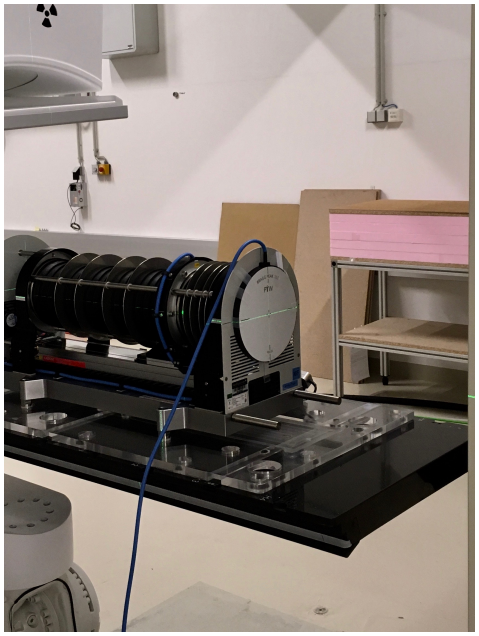

(a) *The experimental setup using PKF with the BPC150 attached to the front*

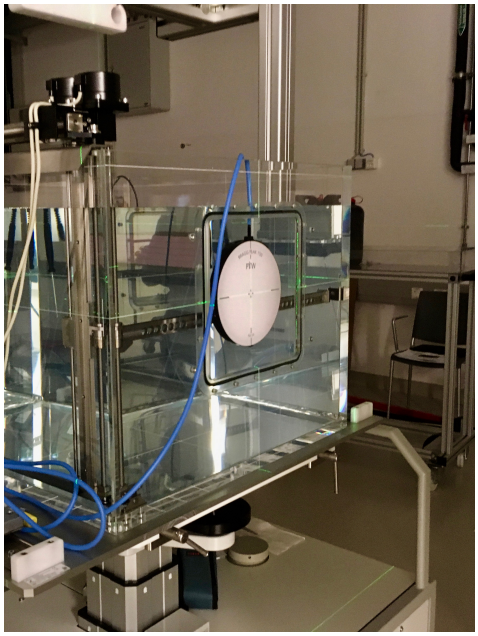

(b) *The experimental setup during proton measurements: here with the BPC150 at a reference depth of 6.35 mm water (5.84 mm WET of the water tanks entrance window and 0.5 mm water)*

Figure 3.2: *Examples of the experimental setup during measurements with protons; the green lines mark the beam isocenter*

BPC150 was mounted in front (see Figure 3.2a) of the entrance window of the PKF and the measurements were repeated with the same beam settings. The particle range (R_{80} in mm[1]) were recorded for both cases and corrected by Equation 3.4 for a deviating water temperature:

$$R = R_{corrected} = \bar{R}_{80} \cdot \frac{\rho_{water}(23°C - (\bar{T}^{meas}_{water} - T^{ref}_{water} \cdot 0.25)}{\rho_{water}(23°C} \tag{3.4}$$

where $\bar{R}_{80}$ is the average of the measured ranges, $\rho_{water}(23°C) = 997.54\ \frac{kg}{m^3}$ is the density of water at $23°C$, $\bar{T}^{meas}_{water}$ is the average of the recorded temperatures of the water during the measurements, $T^{ref}_{water} = 23°C$ is the reference temperature and the factor 0.25 represents the

[1] correspond to the point were the Bragg Peak falls to 80% of its maximum

density variation of water with varying temperature with the unit $\frac{kg}{m^{3}.^{\circ}C}$. The total WET of the BPC150 chamber was then calculated by subtracting the measured range with the BPC150 in front of the PKF (R_{PKF}^{BPC150}) from the initial range value R (Equation 3.5):

$$WET_{total}^{BPC150} = R - R_{PKF}^{BPC150} \tag{3.5}$$

WET of the entrance window ($WET_{entrance}^{BPC150}$): This value was measured using the large water tank (MP3-PL) and the associated mechanism with the MEPHYSTO software to move the chambers in the direction parallel to the proton beam. Alignment was done at iso-center position. The BPC150 was mounted on the movement mechanism of the tank. The laser guide system was used to center the chamber in the plane perpendicular to the beam direction. Thus the chamber center coincided with the beam center. The PTW34070 and the BPC150 were placed successively in the water tank at the same starting depth of 0.5 mm water and moved in the same step increments. The experimental setup with the BPC150 can be seen in Figure 3.2b. The measured ranges were corrected via Equation 3.4. The $WET_{entrance}^{BPC150}$ was determined by

$$\Delta R = R^{34070} - R^{BPC150} \tag{3.6}$$

$$WET_{entrance}^{BPC150} = WET_{entrance}^{34070} + \Delta R \tag{3.7}$$

where ΔR is the range difference between PTW34070 and BPC150, R^{34070} and R^{BPC150} correspond to the ranges measured with the PTW34070 and BPC150, respectively. In the manual of the PTW34070 the $WET_{entrance}^{34070}$ is given as 4 mm [26]. Since deviations between chambers of the same type can occur the $WET_{entrance}^{34070}$ was assessed during equipment commissioning at MedAustron using the flipping method, i.e. the range was measured twice; once the entrance window facing the beam and once the backside of the chamber was facing the beam. These measurements resulted in a entrance window thickness of 4.05 mm.

3.4 Cross calibration in proton beams

The cross calibration procedure in proton beams was done in a two step procedure. The Roos chamber was used to cross calibrate the BPC150. However, as only the Farmer chamber was

calibrated by a standard laboratory in a ^{60}Co beam, first the Farmer and the Roos chamber had to be cross calibrated. This first step was already done by others before this MSc thesis project started.

The cross calibration procedure in proton beams was very similar to the one performed in ^{60}Co radiation (see Chapter 3.2), with the major difference that the the beam quality correction factor k_{Q,Q_0} was not unity. Thus, Equation 3.3 was adapted to correspond to proton beams:

$$N_{D,w,cross}^{Roos} = \frac{M_{Farmer} N_{D,w,Q_0}^{Farmer}}{M_{Roos}} \cdot k_{Q_{cross},Q_0} \tag{3.8}$$

where M_{Farmer} and M_{Roos} are the electrometer readings of the Farmer and the Roos chamber with the respective calibration factors $N_{D,w}^{Farmer}$ and $N_{D,w}^{Roos}$. Values of the beam quality correction factor can be extracted from literature ([18]). For the Farmer chamber type 30013 and a residual range for proton beams (R_{res}) of $19.4 \frac{g}{cm^2}$ the value of the beam quality correction factor (k_{Q_{cross},Q_0}) was 1.029

Subsequently, the Roos chamber served as reference chamber, with known calibration factor, for further cross calibrations in proton beams.

The BPC150 was then cross calibrated against the Roos chamber. The beam quality correction was already applied during calibration of the Roos chamber and thus the calibration factor for the BPC150 can be calculated via:

$$N_{D,w,cross}^{BPC150} = \frac{M_{Roos} N_{D,w,cross}^{Roos}}{M_{BPC150}} \tag{3.9}$$

where M_{Roos} and M_{BPC150} are the electrometer readings of the Roos and the BPC150 chamber, respectively.

Experimental setup: Alignment of the water tank MP3-PL was done at iso-center position. The Roos and the BPC150 were mounted successively on the movement mechanism of the tank. The laser guide system was used to center the chambers in the plane perpendicular to the beam direction. Thus the chamber center coincided with the beam center. The reference depth $z_{ref} = 21.3\, mm$ in beam direction to the front wall of the water tank was identical

for both chambers considering the differences in the WET of the chamber entrance windows. Factors of uncertainties included uncertainties of the movement precision of the water phantom as well as the uncertainty of the WET of the entrance window of the chamber. However, as the position of both chambers was in the plateau of the Bragg-curve, small discrepancies in the positioning resulted only in minor variations of the signal.The cross calibration in proton beams was performed with the following parameters:

- beam energy: 179.2 MeV
- particles per spot: 54802283
- field size: 19.5 cm $\times$ 19.5 cm
- spot spacing: 2 mm

The cross calibration procedure between the Roos chamber and the BPC150 was performed at the same major key beam parameters as the aforementioned cross calibration between the Farmer chamber and the Roos chamber.

The cross calibration procedure was the same as described in Section 3.2 with irradiating the chamber with the known calibration factor before, and afterwards the chamber of interest, followed by the first chamber again. The first step was performed twice, as was the second step. The third step was only performed once, as the reading did not change from the first reading. More measurements for betters statistical accuracy were not possible due to limited beam time.

3.5 Dose area product measurements

Two methods were used to determine the DAP. The first method used a single layer scanned field, which needed to be large enough to guarantee LCPE. It was first proposed by Hartman *et al.* [37] and will therefore be addressed as the Hartman method (abbreviated HM) throughout this work. The dose area product DAP_{HM} was calculated via:

$$DAP_{HM} = MN_{D,w,cross}(LAIC)\Delta x\Delta y \tag{3.10}$$

where M is the reading of the chamber, $N_{D,w}$ is the calibration factor as presented in the second step of Chapter 3.4, specifically through Equation 3.9, $\Delta x \Delta y$ corresponds to the spacing of the beamlets in x- and y-direction.

Necessary conditions for this equation to hold include

i. constant beamlet spacings in the lateral directions

ii. a uniform lateral profile of the scanned field and

iii. a constant number of particles in each beamlets

The nominal spot spacing $dx \cdot dy$ was 2 mm $\times$ 2 mm. However, the distance from the iso-center to the scanning magnets ($d_{ScaMag1}$ and $d_{ScaMag2}$) had to be considered. Taking the reference depth (d_{ref}) into account the actual spot spacing was calculated via:

$$\Delta x \Delta y = dx \cdot \frac{d_{ScaMag1} + d_{ref}}{d_{ScaMag1}} \cdot dy \cdot \frac{d_{ScaMag2} + d\text{–}ref}{d_{ScaMag2}} \tag{3.11}$$

With the following values the spot spacing $\Delta x \Delta y$ in IR1 was 4.023 mm:

- $dx = dy = 2\ mm$
- $d_{ScaMag1} = 7400\ mm$
- $d_{ScaMag2} = 7600\ mm$
- $d_{ref} = 20\ mm$

Table 3.1: *Overview of the measurements investigating the DAP; # stands for the number of measurements and NPS for the number of particles per spot*

	18.04.2018	04.08.2018		
	BPC150	BPC150	34070 SN124	34070 SN125
# 15 $\times$ 15	2	–	–	–
# 18 $\times$ 18	2	–	–	–
# 19 $\times$ 19	2	–	–	–
# 19.5 $\times$ 19.5	–	2	1	1
# SB: $1 \cdot 10^{10}\ NPS$	5	5	5	5
# SB: $3 \cdot 10^{10}\ NPS$	5	5	5	5
# SB: $7.5 \cdot 10^{10}\ NPS$	3	3	5	3

The second method used only a single beamlet directed at the center of the chamber and the recorded dose needed then to be integrated over the whole active area of the chamber ($A_{Chamber}$). This method will be addressed as the single beam (SB) method. The corresponding calculation for the dose area product DAP_{SB} was calculated as follows:

$$DAP_{SB} = MN^{LAIC}_{D,w,cross} A_{Chamber} = MN^{LAIC}_{DAP,w,cross} \tag{3.12}$$

$$N^{LAIC}_{DAP,w,cross} = N^{LAIC}_{D,w,cross} A_{Chamber} \tag{3.13}$$

where M is the reading of the chamber and $N_{D,w,cross}$ is the calibration factor as presented in Chapter Equation 3.9 [38].

Further the DAP was normalized to the number of particles per spot (NPS). The DAP listed in Chapter 4.5 is always in relation to the NPS.

The measurements investigating the DAP were performed on two dates:

- April, 18th 2018: only BPC150 was investigated
  - Hartman method: two irradiations with each of the following field sizes[2]:
    - 15 cm $\times$ 15 cm
    - 18 cm $\times$ 18 cm
    - 19 cm $\times$ 19 cm
  - Single beam method: varying number of measurements (for details see Table 3.1) with the following NPS
    - $1 \cdot 10^{10}$
    - $3 \cdot 10^{10}$
    - $7.5 \cdot 10^{10}$

[2]The purpose of different field sizes was to establish the field size necessary to achieve secondary particle equilibrium and thus fulfill the conditions to apply the HM

- August 4th 2018: PTW34070 SN124, SN125 and BPC150 were investigated
  - Hartman method: two irradiations for the BPC150 and one for the other chamber with a field size of:
    - 19.5 cm $\times$ 19.5 cm
  - Single beam method: varying number of measurements (for details see Table 3.1) with the following NPS
    - $1 \cdot 10^{10}$
    - $3 \cdot 10^{10}$
    - $7.5 \cdot 10^{10}$

Table 3.1 provides an additional overview of the measurements done in order to investigate the DAP.

For the Hartman method the beamlet energy was 179.2 MeV with 54802283 particles per spot and a beamlet spacing $\Delta x \Delta y$ of 4.023 mm^2 according to Equation 3.11.

The measurements with the single beam incident on the chamber center was performed with beamlet energies of 179.2 MeV.

Experimental setup: The placing of the water tank, as well as the alignment of the chamber in all three spatial directions was identical to the setup during the measurement of the $WET_{entrance}$ (see Section 3.3 and Figure 3.2b). The chambers were not moved during the investigation. The measurements were done in water.

3.6 Dose-response maps

3.6.1 Principle

As LAICs can have a non-uniform response over their respective active area, this effect needs correction when performing small field dosimetry. This is especially important for a chamber cross calibrated in a broad field, which is then used for small field dosimetry [22]. The goal of this investigation was to find the correction factor k_{NU} (see Equation 3.16), which corrects for the heterogeneity of the chambers response. An abbreviated derivation of the process,

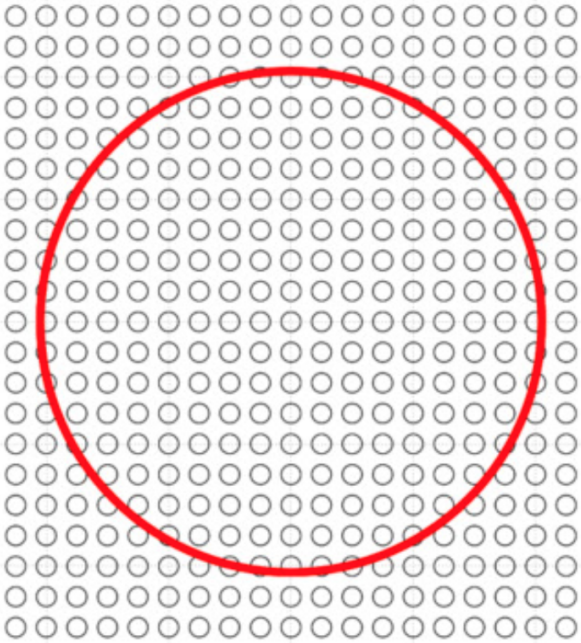

Figure 3.3: *Schematic scan pattern for determination of the non-uniform response of the LAIC under investigation (illustrated by the red circle) [22]*

which leads to k_{NU} will be provided in the following (for the detailed description see [22]).

The relative response as a function of position $r(x, y)$ was normalized to the average response over the whole active area. This normalization was needed as the cross calibration was performed in a large field incorporating the whole active area (A) of the chamber.

$$r(x, y) = \frac{AR(x, y)}{\iint_A R(x, y)\, dx\, dy} \tag{3.14}$$

$R(x, y)$ represents the response of the chamber to a theoretical, dimensionless pencil beam of non-scattering particles at a position (x, y). Taking further into account the off-axis ratio of the calibration field subject to the position (x, y), due to the non-uniformity of the of the beam profile, the non-uniformity corrected (nuc) DAP for a single beamlet ($DAP_{SB,NUC}$) was then calculated via:

$$DAP_{SB,NUC} = DAP_{SB} \times \frac{\iint_A D_{w,SB}(x,y)\,dx\,dy}{\iint_A r(x,y) D_{w,SB}(x,y)\,dx\,dy} \tag{3.15}$$

where DAP_{SB} is the dose area product for a single beamlet as defined in Equation 3.12 and $D_{w,SB}$ is the dose in water for a single beamlet. Equation 3.15 can be further simplified by expressing the last term as the non-uniformity correction factor k_{NU}:

$$k_{NU} = \frac{\iint_A D_{w,SB}(x,y)\,dx\,dy}{\iint_A r(x,y) D_{w,SB}(x,y)\,dx\,dy} \tag{3.16}$$

The determination of $R(x,y)$ then allows for the creation of response correction maps.

3.6.2 Alignment and edge correction

The alignment of the center point of the chamber with the beam exit window of the collimator was only done visually for the BPC150. Thus, the need arose to correct for possible misalignment. This was done based on the data and the assumption, that the active area diameter, given by the manufacturer, is accurate. The alignment for the other chambers was checked before the recording of the DRM by using self developing radiochromic film. During the irradiation with proton beams, the alignment was done using IR1's laser guide system.

The step increment was 5 mm in photon beams and 10 mm in proton beams. Measurements close to the edge of the active area of the investigated LAIC could lead to a decreased response, as only part of the beam hits the actual active area. This had to be treated differently than an under-response of the chamber. To correct for this effect, the actual part of the beam hitting the active area had to be calculated. A Gaussian beam profile for both photon and proton beams was assumed with FWHM of 2.455 mm and 13.633 mm, respectively (see Figure 4.2).

To correct for the response at the edge of the chamber, the following steps were taken:

- Every measurement point outside of the chamber radius was set to 0
- Every measurement point inside the chamber radius minus half of the FWHM was set to 1

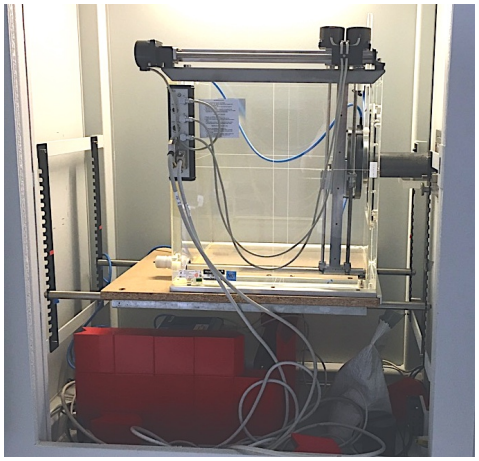

(a) *The experimental setup in the Yxlon X-ray source*

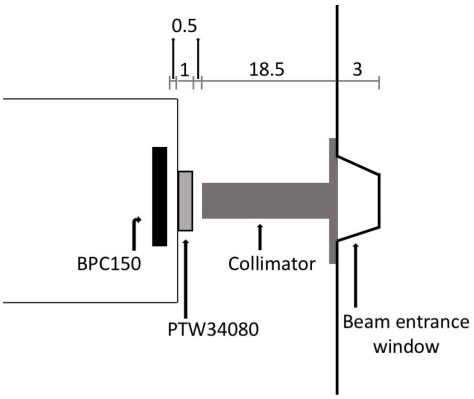

(b) *Schematic depiction of the experimental setup in the Yxlon X-ray source. All units are in cm.*

Figure 3.4: *Experimental setup for the determination of the dose response maps in X-radiation*

- For all measurement points which are now unequal 0 or 1, the proportion of the beam incident on the chamber was calculated and set in relation to the measured response. Thus, a correction factor was calculated. The reciprocal of this value was then noted for further use (to avoid problems due to dividing by 0)
- Lastly, the original measurement points were multiplied with the corrected ones.

3.6.3 Experimental setup

Photon beams: The experimental setup can be seen in Figure 3.4a, and Figure 3.4b provides a schematic representation. As can be seen, the water phantom was placed inside the steel container of the X-ray unit on a wooden plate. The height was chosen in such a manner, that the entrance window of the water phantom was at the same height as the beam exit window of the X-ray source. The distance was 41 cm, measured from the inside bottom of the steel container to the top of the wooden plate.

The collimator was attached in front of the beam exit window with an in-house built anchorage (see Figure 2.2b). The BPC150 was mounted with its custom-made holder on the movement mechanism of the water phantom, while the transmission monitor chamber was

mounted with a telescope holder between the BPC150 and the collimator. The center of both the chamber under investigation as well as the transmission monitor chamber was aligned with the beam exit opening of the collimator. The distance BPC150 to the X-ray source filter was 23.5 cm. The setup was the same for the PTW34070.

The chamber under investigation was moved remotely using the MEPHYSTO software in 5 mm increments. Due to restricted space in the x-ray unit it was not possible to perform the measurement for the whole active area of the BPC150 in one run. Therefore, first one side was irradiated, followed by turning the chamber upside down and irradiating the other side. The irradiation of the PTW34070 could be performed for the whole active area due to its smaller dimensions. The scan pattern is provided in Figure 3.3.

The beam size produced by the collimator was measured using radiochromic EBT3 films. The hereby determined dimensions of the spot will be used to approximate a Gaussian shaped beam profile.

The homogeneity of the chambers was investigated at X-ray tube settings of 200 kV, 20 mA and a focal spot of 5.5 mm. The movement increments were 5 mm with a measurement time of 0.5 s for each spot. The BPC150 was irradiated three times for both halves, while the chambers of type PTW34070 (SN118 and SN124) were irradiated twice.

As already mentioned, the size of the BPC150 did not allow to assess the whole active area. Thus, left and right side of the chamber were irradiated separately. With the chosen step increment a total length of 9 cm in C-direction and 18 cm in B-direction was scanned (for axis direction see Chapter 2.3 and Figure 2.3a). This resulted in a total of 1406 measurement points for both halves of the BPC150, where about 700 points lay within the chambers active area

The PTW34070 was scanned for a total length of 10.5 cm in C-direction and 11 cm in B-direction. This made for a total of 506 measurement points for each chamber where approximately 210 points were within the chambers active area.

Proton beams: The BPC150 was also measured in proton beams to confirm the response gathered by the investigation in photons is transferable to proton beams.

The placing of the water tank, as well as the alignment of the chamber in all three spatial directions was identical to the setup during the assessment of the $WET_{entrance}$ (see Section 3.3 and Figure 3.2b) with the exception that the tank was not filled with water. The beam energy used was 252.7 MeV. Due to the usage of the large water phantom (MP3-PL), the

whole active area of the chamber could be irradiated. The chamber was moved in the plane perpendicular to the beam over an area of 20 cm $\times$ 20 cm in 10 mm increments. Thus, the number of total measurement points was 411 and about 170 points were within the active area of the chamber. The measurement time in the MEPHYSTO software was set at 0.5 s with a spill by time setting.

3.7 Energy variation

Section 3.6 describes the process of recording dose response maps in order to incorporate the different responses of the chambers over their respective active area. The process of recording these maps is cumbersome. Thus a simpler way of gathering the necessary information to correct for differences in response would be appreciated.

The spot size of the beam changes with varying energy. It is smaller for high energy particles and larger for low energy particles. According to [33] the FWHM of a spot with a proton beam energy of approximately 62.4 MeV is 21 mm, whereas the FWHM at a proton beam energy of around 250 MeV is 7 mm. Thus, also a varying size of the active area of the chamber is irradiated. When comparing two chambers of the same type, this method potentially offers an quick way to check if there is a difference in response. The idea was to plot the gathered DAP against the energy for each chamber and to also check the absolute and relative differences in the readings. This information has the potential to give indications concerning the homogeneity response of the chamber.

Different methods were used to evaluate the results of the measurements with varying beam energy:

- The difference in response relative to the individual maximum (R_{IM}) at different energies of one chamber against another (e.g. A and B) was compared in the following manner:

$$\begin{gathered} \Delta R_{IM} = (R_{IM}(E_i) - R_{IM}(E_j))_A \\ with \\ \Delta R_{IM} = (R_{IM}(E_j) - R_{IM}(E_i))_B \end{gathered} \tag{3.17}$$

  where $R_{IM}(E_j - E_i)$ stands for the difference in response for two consecutive energies (see Chapter 4, Table 4.10)

- The respective measurement outcome was normalized to both the highest and the lowest value of each chamber and plotting the result. Here the attention was given to the divergence of the response, when going to higher or lower energy respectively.
- The difference in response of the chambers when normalizing them to the highest response of all chambers was investigated. During this evaluation also the relative differences in response of different chambers at the same beamlet energy (ΔR_{OM}) was investigated (see Chapter 4, Figure 4.10 and Figure 4.11):

$$\Delta R_{OM} = R_{OM}(E)_A - R_{OM}(E)_B \tag{3.18}$$

  where $R_{OM}(E)_A$ stands for the response of chamber A normalized to the overall maximum response of all chambers.

These measurements were performed on April 18th and August 4th 2018 for the BPC150. Furthermore, on August 4th 2018 also the chambers PTW34070 with SN124 and SN125 were investigated. Either the same chamber (as is the case with the BPC150) or different chambers of the same type (PWT34070 SN124, SN125) were compared.

Experimental setup: The placing of the water tank, as well as the alignment of the chamber in all three spatial directions was identical to the setup during the assessment of the $WET_{entrance}$ (see Section 3.3 and Figure 3.2b). The chambers were not moved during the investigation. The measurements were performed in water.

3.8 Measurements in carbon beams

The characteristics of the BPC150 irradiated with carbon ion beams was investigated in comparison to two other chambers: the PTW34070 and the PTW34073. Thus, there is a comparison between a small chamber, the PTW34073 with an active diameter of around 40 mm, a medium sized chamber, the PTW34070 with an active diameter of around 82 mm and a large chamber, the BPC150 with an active diameter of around 147 mm. The larger area of the BPC150 allows for more accurate measurements of both larger spot sizes (with beams of lower energy) and the fragmentation tail (where the dose is administered by secondary particles).

Due to the larger active area of the BPC150 large spot sizes (with beams of low energy) or the distal falloff, can be measured more precisely as no or only a small region of the spot is cut off. The goal of this investigation was to find out whether there is a difference when measuring with different sized chambers. To test this behavior all chambers were used to record IDDs at 4 different energy settings.

Experimental setup: The placing of the water tank, as well as the alignment of the chamber in all three spatial directions was identical to the setup during the assessment of the $WET_{entrance}$ (see Section 3.3 and Figure 3.2b). The chambers were only moved along the beam axis during the investigation (see Figure 2.3a). Four different energy settings were used: 121 MeV, 262 MeV, 327 MeV and 400 MeV.

4 Results

4.1 Cross calibration in ^{60}Co radiation

Table 4.1a shows the k_{TP} corrected readings of measurements taken in ^{60}Co beams, while Table 4.1b provides and overview of the results. The calibration factor of the BPC150 was calculated using Equation 3.3. The dose delivered over a time of five minute was 0.61 Gy.

The 2nd reading (see Table 4.1a) during the measurement with the BPC150 was a potential outlier.

Therefore, an outlier test using Tukey's fence method [39] was performed. This test checks whether values are within or outside certain limits specifically the inner and the outer fence. Values lying beyond the inner fence, but within the outer fence were classified as outliers, while values lying beyond the outer fence were extreme outliers. The summery of the Tukey's fence method based on this data set is given in Table 4.2. Using Tukey's fence method, the 2nd reading (613.01 nC) was classified as an extreme outlier, as it lied beyond the upper outer fence.

The standard deviation of the measurements using the Farmer chamber was < 0.01 nC for the first calibration step and 0.02 nC for the last calibration step. The standard deviation for the measurement with the BPC150 was 0.68 nC including the outlier and 0.23 nC excluding it.

The mean of all readings of the BPC150 deviated by 0.05% from the mean value, when the outlier (613.01 nC) is excluded (see Table 4.1b). Thus, also a 0.05% shift in the calibration factor of the BPC150 was expected.

This lead to a calibration factor for the BPC150 of $(9.96 \pm 0.14) \cdot 10^{-4} \frac{Gy}{nC}$ with and $(9.97 \pm 0.14) \cdot 10^{-4} \frac{Gy}{nC}$ without the outlier. The uncertainty was dominated by uncertainty of the $N_{D,w}$ factor of the Farmer chamber (1.396%).

Table 4.1: *Measurement results of the cross calibration of the BPC150 against the Farmer chamber in ^{60}Co radiation*

(a) *k_{TP} corrected readings for all measurements done during the course of the cross calibration in ^{60}Co radiation*

	k_{TP} corrected readings [nC]				
1st step: Farmer chamber	11.34	11.35	11.34	11.34	11.34
2nd step: BPC150	611.47	613.01	611.78	611.26	611.68
3rd step: Farmer chamber	11.33	11.37	11.33	–	–

(b) *Overview of the results for the cross calibration; AVG stands for average. Thus, the calibration factor ($N_{D,w}$) for further usage of the BPC150 is $(9.97 \pm 0.14) \cdot 10^{-4} Gy/nc$. The uncertainty was dominated by the uncertainty of the $N_{D,w}$ factor of the Farmer chamber (1.396%)*

Chamber type	# of measurements	AVG: k_{TP} corrected readings [nC]	Standard deviation [nC]	$N_{D,w}$ $[\frac{Gy}{nC}]$
Farmer chamber	5	11.34	<0.01	$5.37 \cdot 10^{-2}$
BPC150	5	611.84	0.68	$9.96 \cdot 10^{-4}$
BPC150 [1]	4	611.55	0.23	$\mathbf{9.97 \cdot 10^{-4}}$
Farmer chamber	3	11.34	0.02	$5.37 \cdot 10^{-2}$

[1] Excluding the outlier based on Table 4.2

Table 4.2: *Finding and defining an outlier by applying of Tukey's fence method; V1-V5 represent the from lowest to highest ordered measurement results of the BPC150*

	V1	V2	V3	V4	V5
Ordered readings (BPC150) [nC]	611.26	611.47	611.68	611.78	613.01
1st quartile (Q_1)	$Q_1 = V2$		611.47		
3rd quartile (Q_3)	$Q_3 = V4$		611.78		
Interquartile range (IQR)	$IQR = Q_3 - Q_1$		0.31		
Upper inner fence (UIF)	$Q_3 + 1.5 \cdot IQR$		612.24		
Upper outer fence (UOF)	$Q_3 + 3 \cdot IQR$		612.71		
Lower inner fence (LIF)	$Q_1 - 1.5 \cdot IQR$		611.00		
Lower outer fence (LOF)	$Q_1 - 3 \cdot IQR$		610.54		
Upper outlier	$Value > UIF$				
Extreme upper outlier	$Value > UOF$				
Lower outlier	$Value < LIF$				
Extreme lower outlier	$Value < LOF$				

4.2 Assessment of the water equivalent thickness

Water equivalent thickness of the whole chamber: A proton beam energy of 97.4 MeV was used throughout all WET measurements. The corrected averaged range R in water (see Equation 3.4) measured with the PKF for this energy was 69.99 mm. As the mean value was equal to the measurement readings, the standard deviation was 0 mm, not considering any systematic uncertainties related to the PKF and positioning (e.g. tilted setup). With the BPC150 attached to the front of the PKF, the corrected average range (R_{PKF}^{BPC150}) decreased to 58.75 mm $\pm$ 0.01 mm.

Using Equation 3.5, the result for the total water equivalent thickness of the BPC150 was:

$$WET_{total}^{BPC150} = 11.2\ mm \pm 0.1\ mm$$

The deviation of 0.1 mm arrived mostly from uncertainty of the PKF moving mechanism (0.1 mm) and the standard deviation of the measurement readings of the range with the BPC attached to the front of the PKF. The uncertainty of the WET might be underestimated due to various reasons. The WET of the entrance window was only examined at one point and could be different at another position. The positioning of both the chamber and the PKF could lead to overestimation of the WET if they were not at an exact right angle to the beam (e.g. the chamber is tilted).

An overview of the measurement outcomes is provided in Table 4.3a. Figure 4.1a shows the IDDs. The black lines indicate R_{80} and the purple line represents WET_{BPC150}^{total}.

Water equivalent thickness of the entrance window: The average and corrected range (see Equation 3.4) for the PTW34070 (R^{34070}) was 57.53 mm (standard deviation of 0 mm), again not considering any systematic uncertainties related to the PKF. The range measured with the BPC150 (R^{BPC150}) was 56.95 mm $\pm$ 0.01 mm (averaged and corrected using Equation 3.4). The range difference (Equation 3.6) (ΔR) was thus 0.58 mm. By using Equation 3.7 and the known value of the $WET_{entrance}^{34070}$ (4.05 mm) this lead to a water equivalent thickness of the entrance window of:

$$WET_{entrance}^{BPC150} = 4.6\ mm \pm 0.1\ mm$$

The same considerations concerning the uncertainty of the WET as during the examination of WET_{total}^{BPC150} apply. Table 4.3b shows a summery of the measurements and calculations. Figure 4.1b shows the IDDs for the measurements. The black lines again indicates R_{80}. The green line, which can be seen much better on the zoomed view as shown in Figure 4.1c, represents ΔR.

Table 4.3: *Results for the determination of the water equivalent thickness of the BPC150. StDev stands for standard deviation. The averaged and corrected (see Equation 3.4) ranges:*
(a) *R and R_{PKF}^{BPC150} can be directly inserted in Equation 3.5 to calculate WET_{total}^{BPC150}.*
(b) *R^{34070} and R^{BPC150} can be directly inserted in Equation 3.6 to calculate ΔR, which was then used in Equation 3.7 to assess $WET_{entrance}^{BPC150}$*

(a) *Results for the measurements investigating WET_{total}^{BPC150}*

	Average range [mm]	StDev [mm]	WET_{total}^{BPC150} [mm]
R	69.99	0.00	11.2 mm
R_{PKF}^{BPC150}	58.75	0.01	

(b) *Results for the measurements investigating $WET_{entrance}^{BPC150}$*

	Averaged range [mm]	StDev [mm]	WET_{total}^{BPC150} [mm]
R^{34070}	57.53	0.00	4.6
R^{BPC150}	56.95	0.01	

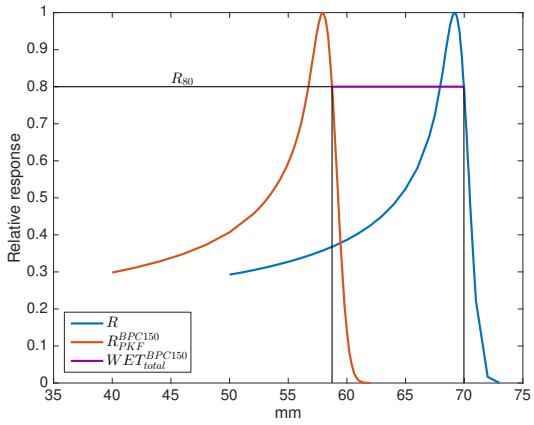

(a) *IDDs for the measurements with the PKF with (orange line) and without (blue line) the BPC in front of the PKF. The black line indicates R_{80} and the lilac line represents WET_{total}^{BPC150}. For a definition of R, R_{PKF}^{BPC150} and WET_{total}^{BPC150} the reader is refered to Chapter 3.3*

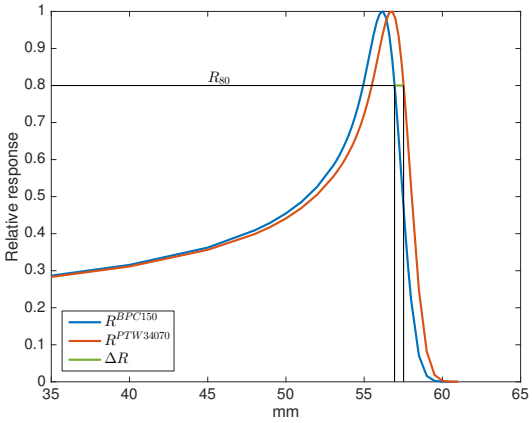

(b) *IDD measurements in the MP3-PL with the BPC150 (blue line) and PTW34070 (orange line). The black line indicates R_{80} and the green line represents ΔR. For a definition of R^{BPC150}, R^{34070} and ΔR, as well as the consequential calculation of $WET_{entrance}^{BPC150}$ the reader is refered to Chapter 3.3*

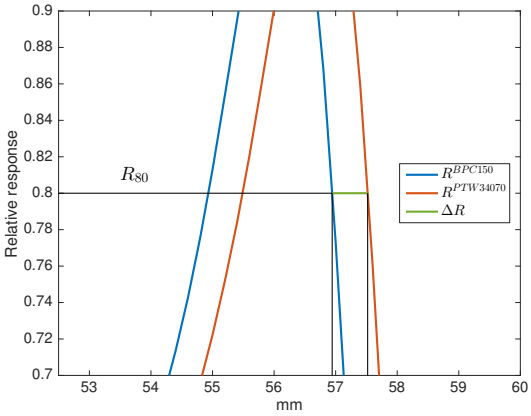

(c) *Zoom of the region of interest of the left Figure (4.1b), to provide a better view of ΔR*

Figure 4.1: *IDDs for the measurements investigating the WET*

4.3 Cross calibration in proton beams

The cross calibration of the Roos chamber against the Farmer chamber for a proton beam energy of 179.2 MeV was performed on October 26th 2016. This resulted in a calibration factor for the Roos chamber of $N_{D,w,cross}^{Roos} = 8.45 \cdot 10^{-2} \frac{Gy}{nC}$. The beam quality correction factor $k_{Q_{cross},Q_0} = 1.029$ was already included.

To determine the cross calibration factor for the BPC150 Equation 3.9 was used. M_{Roos} and M_{BPC150} were the k_{TP} corrected and averaged readings of the Roos chamber and the BPC150, respectively. The calibration factor of the BPC150 was then determined to be $N_{D,w,cross}^{BPC150} = (9.78 \pm 0.14) \cdot 10^{-4} \frac{Gy}{nC}$. Table 4.4 shows an overview of those results.

Table 4.5 provides an overview of the calibration factors of all used chambers.

Table 4.4: *Results for the cross calibration procedure in proton beams of the BPC150 versus the respective results of the Roos chamber; M stands for the averaged and k_{TP} corrected reading and StDev relates to the standard deviation*

	M [nC]	StDev [nC]	$N_{D,w,cross}$ $[\frac{Gy}{nC}]$
Farmer chamber	–	–	$5.37 \cdot 10^{-2}$
Roos chamber	13.84	0.01	$8.45 \cdot 10^{-2}$
BPC150	1196.03	0.73	$9.78 \cdot 10^{-4}$

Table 4.5: *Overview of the calibration factors $N_{D,w}$ in proton beams for the different chambers*

Chamber	Farmer chamber	Roos chamber	PTW34070 SN124	PTW34070 SN125	BPC150
Calibration factor $[\frac{Gy}{nC}]$	$5.37 \cdot 10^{-2}$	$8.45 \cdot 10^{-2}$	$3.14 \cdot 10^{-3}$	$3.23 \cdot 10^{-3}$	$9.78 \cdot 10^{-4}$

4.4 Dose response maps

4.4.1 Photon beams

The uncorrected dose response map (DRM) for the BPC150 can be seen in Figure 4.3a. These maps represent the mean of all three recorded DRMs. As already mentioned, the chamber's size made an irradiation of the whole active area in one run impossible. Therefore, the two halves were investigated separately. This is shown in Figure 4.3a. For each half three measurements were averaged and both halves were normalized to the overall maximum value. The highest standard deviation between the three measurements was 0.60% for the left side and 0.87% for the right side of the chamber. The alignment of the two halves was done during the edge correction.

Figure 4.3b shows the DRM after aligning, edge correction and combination of the halves. Due to the small spot size of the collimated X-ray beam the influence of the edge correction was limited.

The response in the center (i.e. a section of approximately rectangular shape with a side length of around 15 mm) of the chamber was by about 4-6% lower than the maximum response. This was followed by a ring shaped region with the relative lowest response of up to -10% at a chamber radius of about 18 mm to 40 mm. The highest response was towards the physical edge of the chamber. A plot of the radial response is provided in Figure 4.7 for all measured chambers. Note that the values were normalized to the measurement point of highest response.

The uncorrected DRM for the chamber type PTW34070 (SN118 and SN124) can be seen in Figure 4.4a and Figure 4.5a, respectively. Both maps represent the mean of the measurements. The maximal standard deviation between the two measurements was 0.25% for the SN118 and 3.76% for the SN124. As only the chambers were exchanged, whereas the setup and measurement routine did not change during the irradiations, the high standard deviation of the SN124 is addressed in Chapter 5.

Figure 4.4b and Figure 4.5b show the DRM after the edge correction.

In both chambers the highest response was in the center. Radially outward the response decreased by up to 10%, similar to concentric circles. The SN124 had an outlier at the po-

sition [-30,0], where the response was 2% higher compared to its neighboring measurement points.

4.4.2 Proton beams

The uncorrected DRM of the BPC150, when irradiated with proton beams in air, can be seen in Figure 4.6a. As only one measurement was performed, no measurement uncertainty is given. Due to the lower resolution (i.e. the larger spot size: Figure 4.2b) the response map was less detailed (compared to Figure 4.3), but showed the same trend: a lower response in the center, which was increasing towards the edge. However, the higher response in the chamber center, as can be seen on the DRM gathered in photon radiation (4.3), was not visible in proton beams. This is discussed in detail in Chapter 5.

Figure 4.6b shows the edge corrected DRM for proton beams. Here the impact of the correction can be seen clearly, due to both the increased spot size compared with the photon beams and the longer step increment.

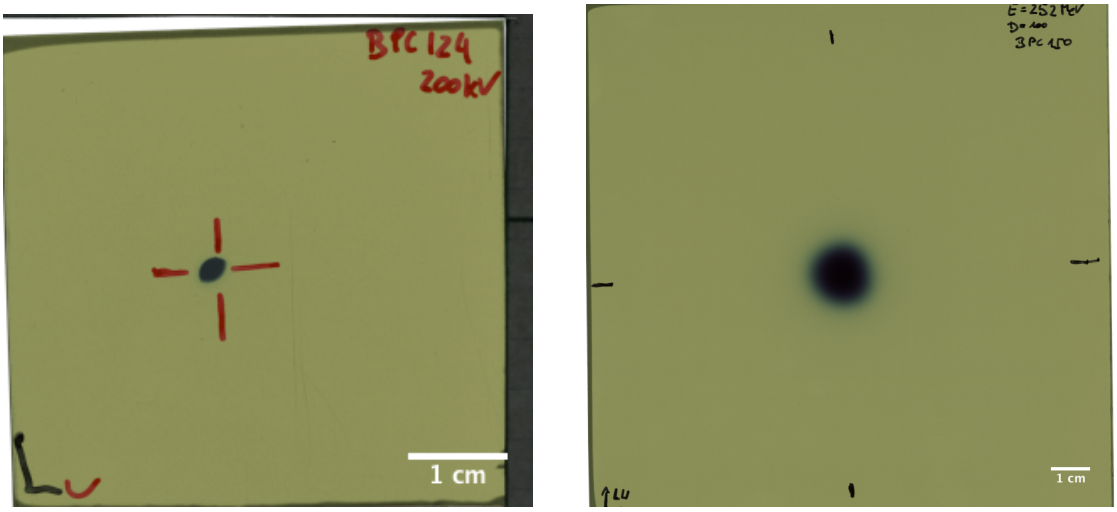

(a) *The developed radiochromic film when exposed with the collimated photon beam. When approximated as a gaussian beam the FWHM is 2.455 mm*

(b) *The developed radiochromic film when exposed to a proton beam with an energy of 252.7 MeV. The FWHM is 13.633 mm*

Figure 4.2: *Comparision of the spot size determined for both photon and proton beams*

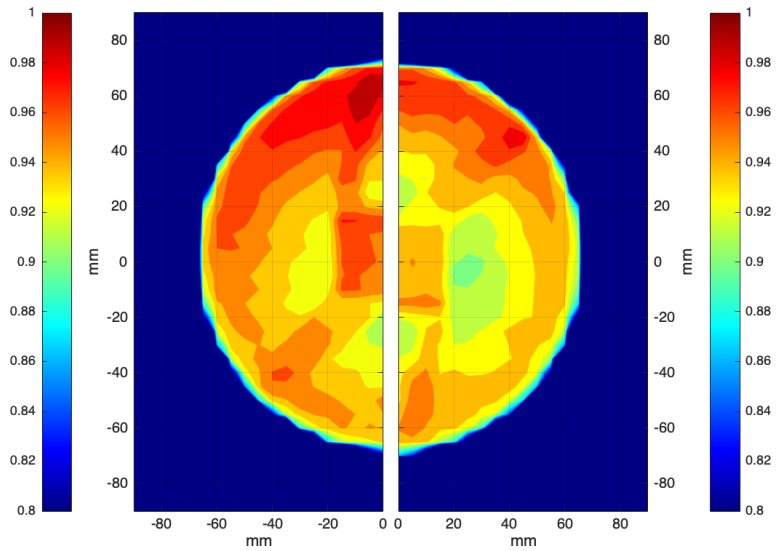

(a) *Original DRM of the BPC150*

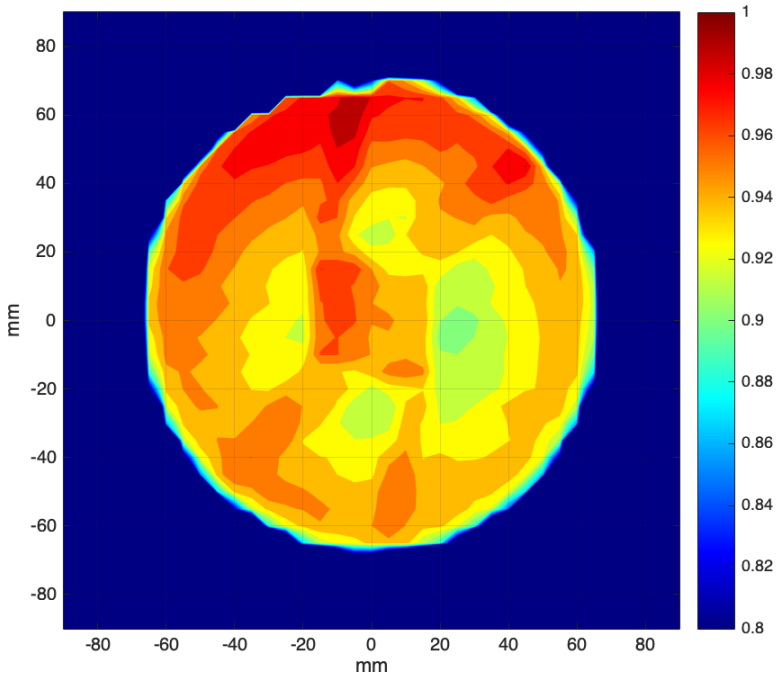

(b) *DRM of the BPC150 after edge correction, alignment and combination of the two halves*

Figure 4.3: *Dose response maps for the BPC150 in X-radiation*

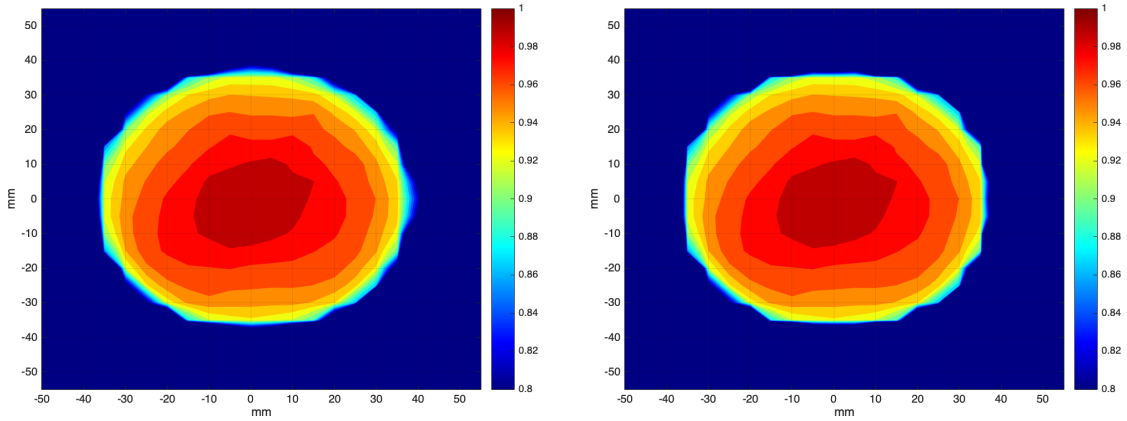

(a) *Original DRM for the PTW34070 SN118*

(b) *DRM of the PTW34070 SN118 after edge correction*

Figure 4.4: *Dose response maps for the PTW34070 SN118 in X-radiation*

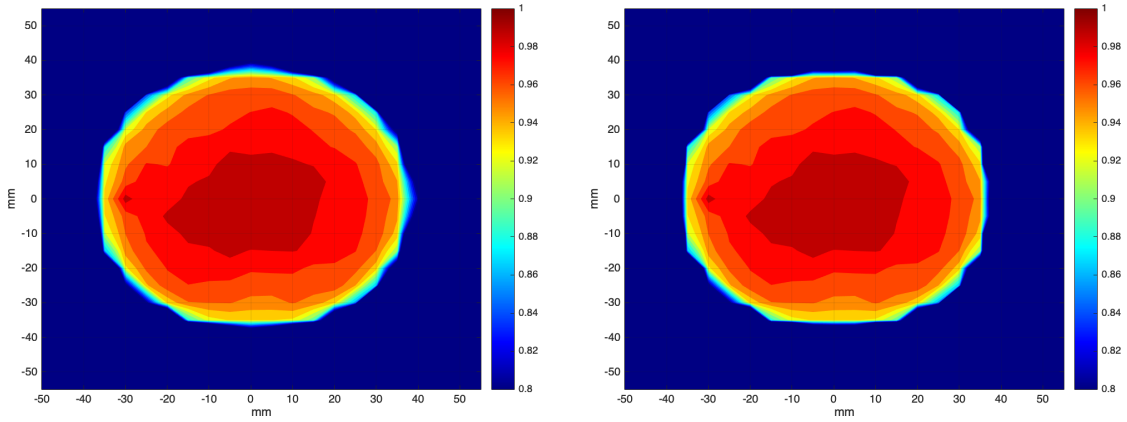

(a) *Original DRM for the PTW34070 SN124*

(b) *DRM of the PTW34070 SN124 after edge correction*

Figure 4.5: *Dose response maps for the PTW34070 SN124 in X-radiation*

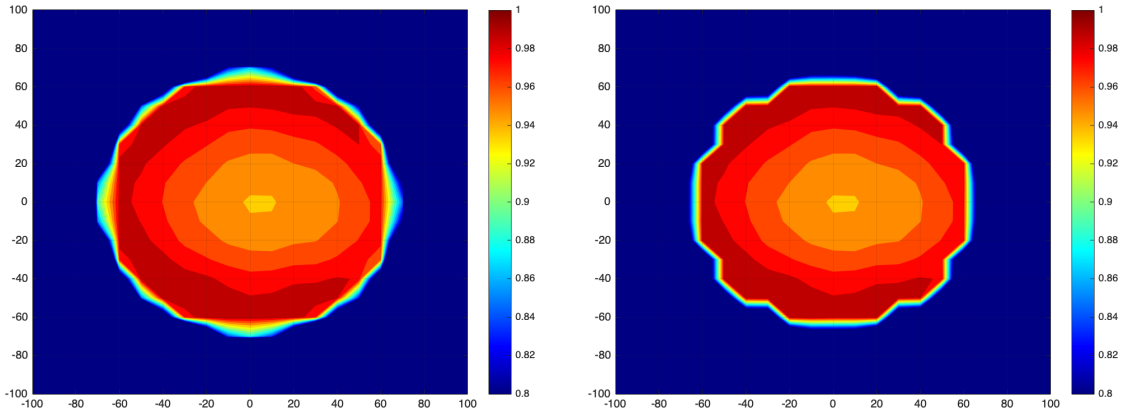

(a) *Original map for the BPC150 in proton beams*

(b) *DRM of the BPC150 when irradiated with proton beams after the edge correction*

Figure 4.6: *Dose response map for the BPC150 in proton radiation*

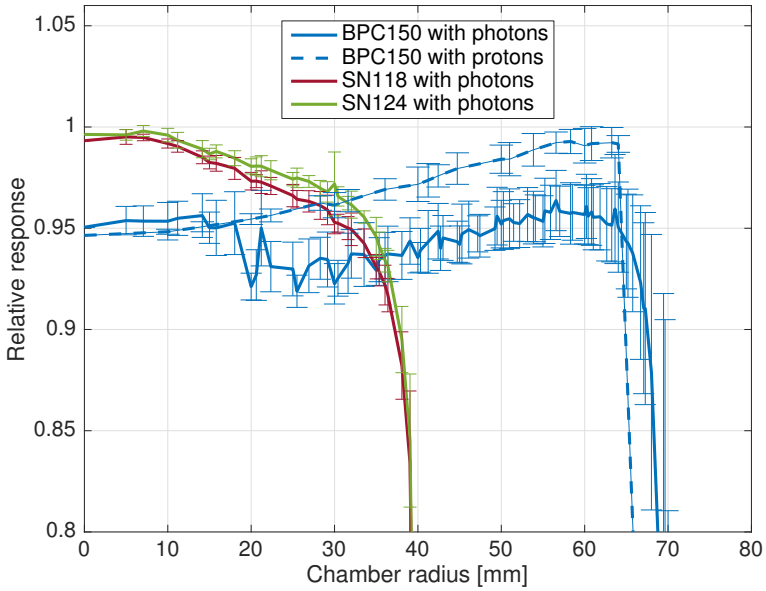

Figure 4.7: *Relative response as a function of the chamber radius for all measured chambers*

4.4.3 Non-uniformity correction factor

The non-uniformity correction factor, k_{NU}, was calculated using the methodology outlined in Chapter 3.6.1 for a spot with a diameter of 13.63 mm incident on the chamber center, thus corresponding to the spot measured in a proton beam energy of 252.7 MeV (see Figure 4.2b). The results are presented in Table 4.6. As expected, both the PTW34070 SN118 and 124 showed a k_{NU} lower than 1, representing the relative over-response in the chamber center. The k_{NU} for the BPC150 evaluated in proton beams was greater than 1 and thus showed the expected behavior: an under-response in the chamber center.

The k_{NU} of the BPC150 evaluated in photon beams had a value of 0.992, showing a slight over-response in the center of the chamber. This is evident, when studying Figure 4.3b. The steep decrease in response (up to 10%) starts at a radius of 18-20 mm.

Table 4.6: *The non-uniformity factors k_{NU} for all investigated chambers. p^+ stands for protons and γ for photons*

	Medium response[%]	Response in chamber center [%]	k_{NU}
SN124	0.957	0.993	0.964
SN118	0.967	0.995	0.971
BPC150 (p^+)	0.977	0.948	1.031
BPC150 (γ)	0.946	0.954	0.992

4.5 Dose area product measurements

For the following results the non-uniformity correction, as explained in Chapter 3.6, has not been applied.

April 18th 2018: As already explained in Chapter 3.5 the measurements with the BPC150 investigating the Hartman DAP method were performed twice for varying field sizes and the measurements with single beams were repeated with varying NPS. Table 3.1 provides and overview of the DAP measurements and Table 4.7 summarizes the measurement outcomes for April 18th 2018. The calibration factor used was $N_{D,w,cross}^{BPC150} = (9.78 \pm 0.14) \cdot 10^{-4} \frac{Gy}{nC}$ as measured in Chapter 4.3. The DAP was calculated following Equation 3.10 for the Hartman method and following Equation 3.12 for the single beam method. The outcomes of both cases were normalized to the number of particles per spot.

The BPC150 was irradiated with varying field sizes of 15 cm $\times$ 15 cm, 18 cm $\times$ 18 cm and 19 cm $\times$ 19 cm. Normalized to the reading for the 19 cm $\times$ 19 cm field the decrease was 0.005% for the 18 cm $\times$ 18 cm field and 1.024% for the 15 cm $\times$ 15 cm field Further, the measurement outcomes of the 15 cm $\times$ 15 cm field were omitted for DAP evaluation with the HM.

During the SB measurements the chamber was irradiated with varying number of particles per spot and the deviation between the DAP with different NPS for the SB method was within the measurement uncertainty.

Comparing the results gathered via the Hartman method to those of the single beamlet method resulted in a difference of 6.12%. This result can be compared to the k_{NU} factor as calculated in 4.4.3 and is addressed in Chapter 5.

August 4th 2018: The DAP was measured with 3 chambers, the BPC150 and two chambers of type PTW34070 (SN124 and SN125). Both methods were investigated for all chambers and the number of measurements done for each chamber can be seen in Table 3.1.

The calibration factor used for the BPC150 was $N_{D,w,cross}^{BPC150} = 9.78 \cdot 10^{-4} \frac{Gy}{nC}$ (see Chapter 4.3), the one used for the PTW34070-SN124 was $N_{D,w,cross}^{SN124} = 3.14 \cdot 10^{-3} \frac{Gy}{nC}$ and the PTW34070-SN125 has a calibration factor of $N_{D,w,cross}^{SN125} = 3.23 \cdot 10^{-3} \frac{Gy}{nC}$. An overview of the calibration factors is provided in Table 4.5. The DAP was calculated using the Hartman

Table 4.7: *Results for both the Hartman and the single beam measurements investigating the DAP on April 18th 2018 for the BPC150; M stands for the averaged and k_{TP} corrected reading, StDev relates to the standard deviation*

	M [nC]	StDev [nC]	DAP $[nGy \cdot mm^2]$	$\overline{DAP}$ $[nGy \cdot mm^2]$	StDev $[nGy \cdot mm^2]$
Hartman method					
15 cm × 15 cm	1123.44	0.10	80.65		
18 cm × 18 cm	1135.01	0.10	81.48	81.49[1]	<0.01[1]
19 cm × 19 cm	1135.07	0.02	81.49		
SB method					
$1 \cdot 10^{10}$ NPS	46.09	0.01	76.51		
$3 \cdot 10^{10}$ NPS	138.27	0.00	76.50	76.50	<0.01
$7.5 \cdot 10^{10}$ NPS	345.69	0.06	76.51		

[1] Does not include the result of the 15 cm × 15 cm field

method (Equation 3.10) and the single beam method (Equation 3.12). The results were normalized to the NPS. Table 4.8 provides an overview of the measurement outcomes.

The SB measurements were done with a varying number of particles per spot. The deviation between the DAP with different NPS for the SB method was within the measurement uncertainty.

Comparing the Hartman method to the single beam method for each chamber individually resulted in the following deviations:

$$BPC150 \longrightarrow \Delta: \ 8.71\%$$
$$PTW34070 - SN124 \longrightarrow \Delta: \ 4.14\%$$
$$PTW34070 - SN125 \longrightarrow \Delta: \ 2.03\%$$

The SB results for the BPC150 from August differed by 2.24% in comparison to the April measurements, which resulted in a drift between both investigated methods by 2.59%.

Table 4.8: *Results for both the Hartman and the single beam measurements investigating the DAP on August 4th 2018 for the BPC150, the PTW34070-SN124 and the PTW34070-SN125; M stands for the averaged and k_{TP} corrected reading, StDev relates to the standard deviation*

(a) *Results for the DAP measurements on August 4th for the BPC150*

	M [nC]	StDev [nC]	DAP $[nGy \cdot mm^2]$	$\overline{DAP}$ $[nGy \cdot mm^2]$	StDev $[nGy \cdot mm^2]$
Hartman method					
19.5 cm × 19.5 cm	1141.67	0.00	81.93	81.93	–
SB method					
$1 \cdot 10^{10}$ NPS	45.05	0.00	74.74		
$3 \cdot 10^{10}$ NPS	135.10	0.00	74.83	74.79	0.04
$7.5 \cdot 10^{10}$ NPS	338.10	0.00	73.79		

(b) *Results for the DAP measurements on August 4th for the PTW34070-SN124*

	M [nC]	StDev [nC]	DAP $[nGy \cdot mm^2]$	$\overline{DAP}$ $[nGy \cdot mm^2]$	StDev $[nGy \cdot mm^2]$
Hartman method					
19.5 cm × 19.5 cm	360.34	–	83.16	83.16	–
SB method					
$1 \cdot 10^{10}$ NPS	48.48	0.01	79.71		
$3 \cdot 10^{10}$ NPS	145.48	0.05	79.74	79.72	0.02
$7.5 \cdot 10^{10}$ NPS	363.54	0.06	79.71		

(c) *Results for the DAP measurements on August 4th for the PTW34070-SN125*

	M [nC]	StDev [nC]	DAP $[nGy \cdot mm^2]$	$\overline{DAP}$ $[nGy \cdot mm^2]$	StDev $[nGy \cdot mm^2]$
Hartman method					
19.5 cm × 19.5 cm	360.13	–	83.12	83.12	–
SB method					
$1 \cdot 10^{10}$ NPS	48.21	0.00	81.43		
$3 \cdot 10^{10}$ NPS	144.60	0.00	81.42	81.43	0.01
$7.5 \cdot 10^{10}$ NPS	361.60	0.00	81.44		

4.6 Dose area product: energy variation

The results of the measurements of single beams concerning the energy variation are summarized in Table 4.9. The comparison of the differences in response as presented in Chapter 3.7, via Equation 3.17 can be seen in Table 4.10. Comparing ΔR_{IM} of different chambers resulted in very similar values. The highest standard deviation was 0.51%. Figure 4.8 shows the DAP relative to the highest DAP ($DAP(E = 62.4\ MeV)$) of each individual chamber. As differences in response at lower energies are omitted when normalizing based on the lowest energies (Figure 4.8), Figure 4.9 provides an overview of the chamber response normalized to the DAP at the highest energy ($DAP(E = 252.7\ MeV)$). The deviation of the response relative to the highest DAP was comparable to the one of the lowest DAP.

Additionally, Figure 4.10 shows the response of the chambers relative to the highest response of all chambers; in this case the PTW34070 SN125. The curve shape was basically the same for all chambers and the deviation in chamber response was similar over the whole range for all chambers with a maximum standard deviation of 1.5%. Figure 4.11 shows the same as Figure 4.10, but the measurements of the BPC150 were averaged. The turquoise lines shows the differences between the chambers, as presented in Equation 3.18. The relative difference between the PTW34070 SN124 and SN125 had the smallest standard deviation of 0.1%, while the standard deviation of the relative difference between both the SN124-BPC150 and SN125-BPC150 was 0.7%.

Table 4.9: *Results for the energy variation for all investigated chambers. The DAP_{norm} was calculated using the SB method (see Equation 3.12 and normalizing it to the number of particles per spot*

	BPC150				PTW34070			
	April		August		SN124		SN125	
E $[MeV]$	DAP_{norm} $[nGy \cdot mm^2]$	StDev	DAP_{norm} $[nGy \cdot mm^2]$	StDev	DAP_{norm} $[nGy \cdot mm^2]$	StDev	DAP_{norm} $[nGy \cdot mm^2]$	StDev
252.7	61.88	0.06	62.61	0.06	66.64	0.00	68.10	0.00
232.6	65.04	0.06	65.75	0.00	70.10	0.00	71.57	0.00
202.5	70.76	0.00	71.56	0.00	76.35	0.00	78.08	0.00
179.2	76.47	0.03	74.79	0.00	83.16	0.00	83.12	0.00
132.0	94.71	0.00	95.82	0.06	102.35	0.06	104.63	0.00
79.6	147.51	0.06	149.78	0.06	158.35	0.06	161.85	0.06
72.4	163.37	0.06	166.23	0.06	174.80	0.00	178.66	0.06
62.4	195.68	0.06	200.11	0.06	207.89	0.06	212.29	0.00

Table 4.10: *Difference in relative response at different energies (i.e. relative to the individual maximum intensity), as calculated via Equation 3.17*

				BPC150		PTW34070	
				April	August	SN124	SN125
i	E_i	j	E_j	ΔR	ΔR	ΔR	ΔR
1	252.7	2	232.6	0.02	0.02	0.02	0.02
2	232.6	3	202.5	0.03	0.03	0.03	0.03
3	202.5	4	179.2	0.03	0.03	0.03	0.03
4	179.2	5	132.0	0.09	0.09	0.10	0.10
5	132.0	6	79.6	0.27	0.27	0.27	0.27
6	79.6	7	72.4	0.08	0.08	0.08	0.08
7	72.4	8	62.4	0.17	0.17	0.16	0.16

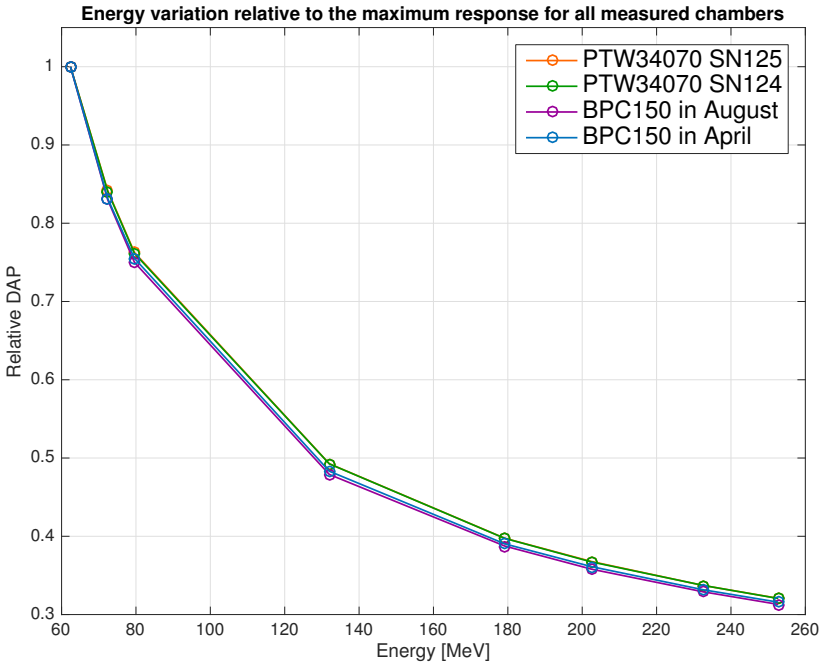

Figure 4.8: *Energy variation normalized to the maximum DAP (i.e. lowest beam energy) for each individual chamber*

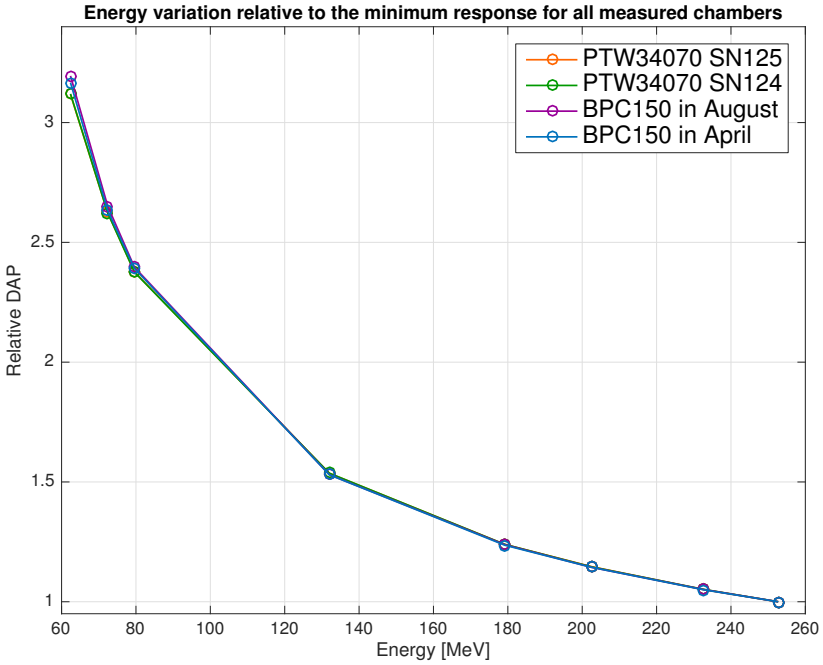

Figure 4.9: *Energy variation normalized to the minimum DAP (i.e. highest beam energy) for each individual chamber*

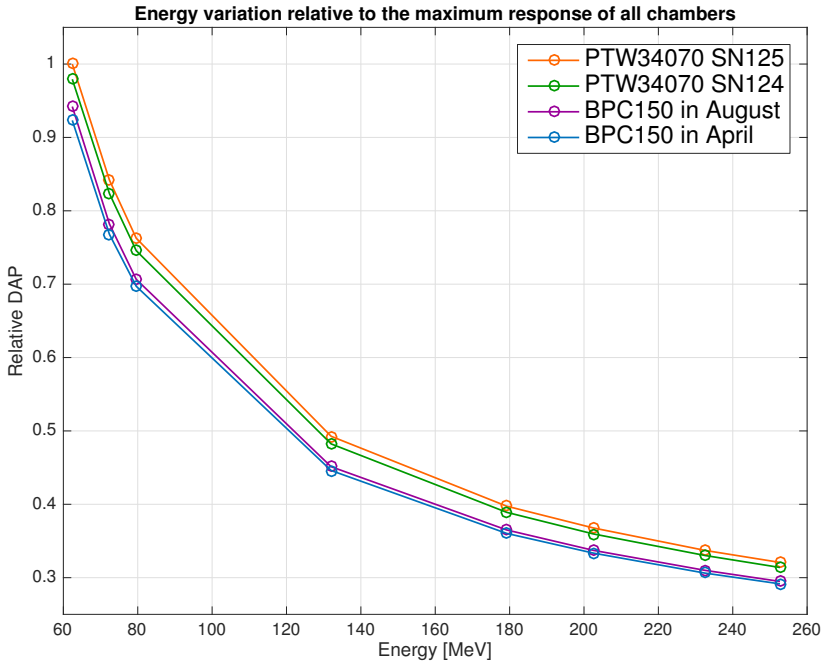

Figure 4.10: *Energy variation normalized to the maximum DAP for all chambers (here the PTW34070 SN125)*

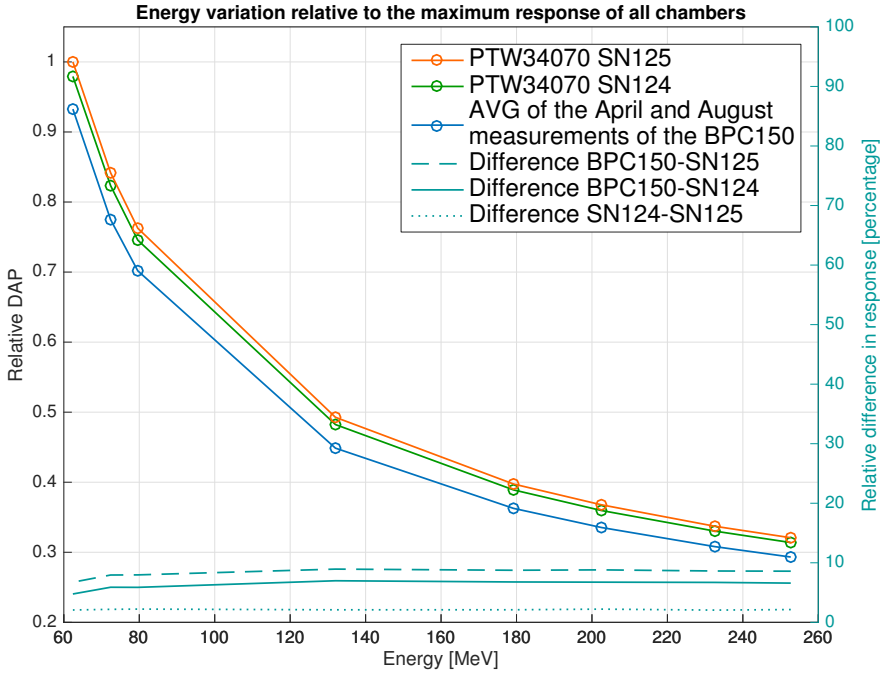

Figure 4.11: *Same as Figure 4.10, but the measurements of the BPC150 were averaged and the turquoise lines provide a representation of the differences between the chambers*

4.7 Measurements in carbon beams

Figure 4.12 shows an overview of the recorded IDDs in carbon beams. As can be seen the fragmentation tail got more pronounced the larger the active area of the chamber is. This was especially distinct at high energies.

Figure 4.13 shows the IDD only for an energy of 400 MeV/u, as well as the relative difference between chambers. The solid turquoise line shows the relative difference between the medium sized chamber (PTW34070) and the large chamber (BPC150), while the dashed turquoise line shows the relative difference between the small chamber (PTW34073) and the BPC150. These curves showed a difference for increasing range up to -150%. As the intensity in these ranges were minimal, those high discrepancies were not pivotal. Thus, the relevant part was at the beginning of the fragmentation tail. The start of the fragmentation tail was determined individually for each energy with the recorded data and was in this context defined to start at a relative response of:

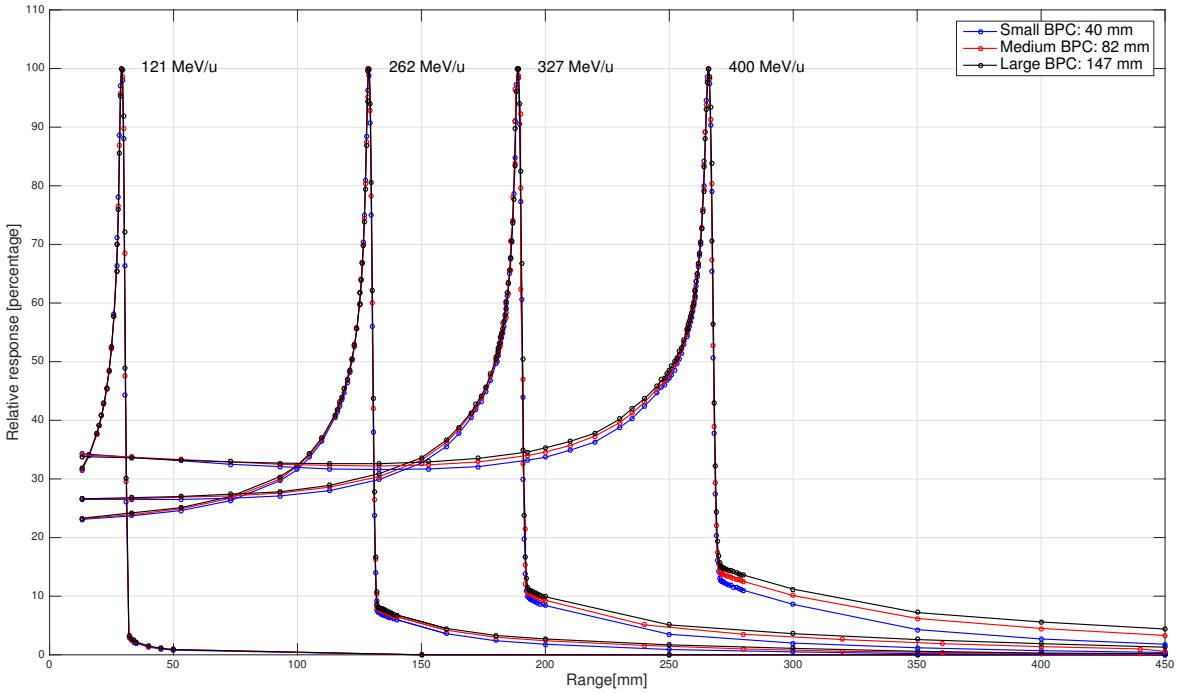

Figure 4.12: *IDDs for the measurement with carbon beams for all used energies and all chambers*

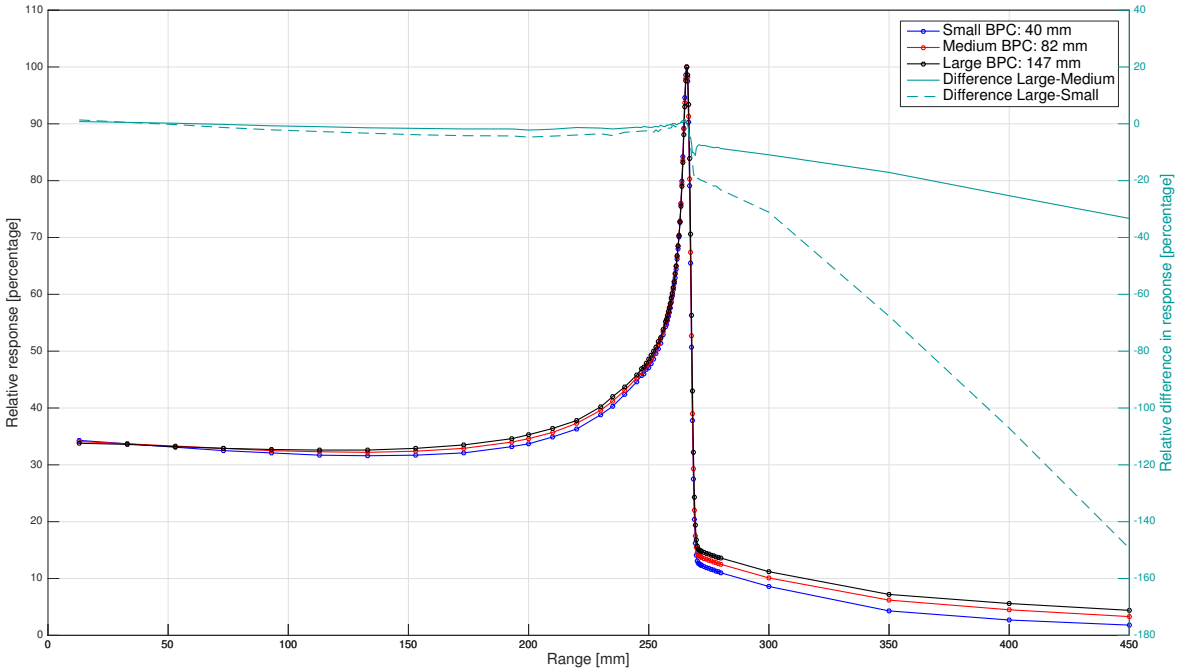

Figure 4.13: *IDDs for the measurements with a carbon beam energy of 400 MeV/u for all chambers. The dotted turquoise lines provides an overview of the relative differences of the measured dose between the medium and the large chamber. The dashed turquoise line provides the same but for the small and large chamber*

- $<$15% for a beam energy of 400 MeV
- $<$12% for a beam energy if 327 MeV
- $<$10% for beam energies of 262 MeV and 121 MeV

The relative differences between chamber response at the beginning of the fragmentation tail for all energies and all chambers are provided in Table 4.11.

The range R_{80} measured with the chambers was gathered and compared as can be seen in Table 4.12. This amounted to 1% in terms of peak dose. In comparison to the small Bragg Peak chamber (type 34073) the difference was even about 20% (2.5-3% in terms of peak dose). In the proximal region of the Bragg peak a difference of 1-2% was observed.

Table 4.11: *Overview of the relative differences between chamber response in carbon beams at the beginning of the fragmentation tail*

Beam energy	Rel. difference medium and large chamber	Rel. difference small and large chamber
400 MeV/u	7.5%	19.6%
327 MeV/u	5.7%	15.1%
262 MeV/u	3.8%	11.1%
121 MeV/u	2.5%	8.6%

Table 4.12: *Comparison of carbon range measurements (R_{80}) gathered with different sized large area ionization chambers for four energies.*

	R_{80}		
Beam energy	34073 (39 mm)	34070 (81 mm)	BPC150 (147 mm)
400 MeV/u	29.95	29.98	30.04
327 MeV/u	129.67	129.75	129.81
262 MeV/u	189.92	190.00	190.06
121 MeV/u	266.97	267.01	267.12

5 Discussion

In this study a prototype large area ionization chamber from PTW was investigated. All information about the prototype chamber (BPC150) was given in personal correspondence with PTW. Therefore, deviations regarding the composition and diameter of the active area can not be excluded. Especially, the exact chamber's size is of high importance for DAP measurements and should thus be investigated by other means as well.

As already mentioned, LAICs with an even larger radius as the well described PTW34070 and PTW34080 (diameter = 81.6 mm) are promising, due to their higher geometric collection efficiency [40] [41] and the higher collection rate for lighter fragments in carbon ion beams.

The largest plane parallel ionization chamber currently on the market is the Stingray (IBA Dosimetry, Schwarzenbruck, Germany) with an active diameter of 120 mm [42]. Comparing the performance of the Stingray to the BPC150 in both DAP and depth dose measurements would be of interest. Not only to investigate whether there is still a benefit when going from a diameter of 120 mm to 147 mm, but also to compare the characteristics of two chambers produced by different vendors.

Complete accordance with IAEA TRS 398 ([18]) could not be achieved during the cross calibration procedure in ^{60}Co radiation. However, the best conformity possible was aspired. For example, IAEA TRS 398 specifies a field size for calibration of 10 cm $\times$ 10 cm, which would not incorporate the full active area of the BPC150. Thus, a larger field size was chosen (i.e. 19 cm $\times$ 19 cm). Additionally, the Farmer chamber was provided with a specific holder, therefore assuring complete enclosure of the chamber in RW3. Such a holder was not available for the BPC150, which was placed free in air with RW3 plates below and above.

Having gathered the calibration factors for the BPC150 in ^{60}Co radiation and in proton beams, allowed the determination of the beam quality correction factor k_{Q_{cross},Q_0} of 0.98. Comparing this value to k_{Q_{cross},Q_0} factors of other chambers given in IAEA TRS 398 and Gomà *et al* (2015) [43] revealed that only for plane parallel ionization chambers k_{Q_{cross},Q_0}

factors were below 1. The k_{Q_{cross},Q_0} value closest to the one of the BPC50 is the NACP Plane Parallel Chamber (IBA Dosimetry, Schwarzenbruck, Germany). Note that not all k_{Q_{cross},Q_0} factors of plane parallel ionization chambers were below 1, as clearly evident by the k_{Q_{cross},Q_0} factor of the Roos chamber of 1.029 also used in this work. Furthermore, k_{Q_{cross},Q_0} factors given in IAEA TRS 398 were recorded in reference conditions, they are highly chamber specific and thus, should be investigated individually by means of either Monte Carlo simulations or experimentally. [43] [44] [45]

The PTW34070 and 34080 chambers are not mentioned in the IAEA TRS 398, therefore a comparison of the k_{Q_{cross},Q_0} factors of these chambers determined within this work to the TRS398 report was not possible. Alternatively, Gomà *et al* (2017) [45] provided k_{Q_{cross},Q_0} for the PTW34070 of 1.001 (E=150 MeV) to 1.011 (E=250 MeV).

In Chapter 3.3 the determination of the $WET_{entrance}$ using the flipping method is outlined. In short, this method measures the WET of the entrance window of any plane parallel chamber by measuring the same particle range twice but flipping the chamber's orientation towards the beam. This approach could not be applied for the BPC150. Due to the holder geometry, the flipped chamber could not be mounted on the moving mechanism of the water tank. Therefore, a relative measurement was employed by using a chamber with a known $WET_{entrance}$.

The BPC150's intended use and also its basic design is similar to the chamber type PTW34070. Thus, it could be expected that the entrance window thickness of the BPC150 was in the same order of magnitude as the $WET_{entrance}$ of the type 34070.

The PTW34080 serves mostly as a transmission monitor chamber and is not water tight. The design is specifically chosen to have a low density limit beam attenuation caused by the monitor chamber.

A non uniform response was recorded for all investigated LAICs. For the BPC150 the same fundamental trend could be observed for both photon and proton measurements: a relatively lower response in the center, which increased towards the chamber edge. However, for the DRM recorded with X-rays the response in the center appeared to be higher and only around the center the response decreased. Comparing the DRM of the BPC150 (Figure 4.3) recorded in photon beams to the response maps of the chambers of type 34070 (Figure 4.4 and 4.5), two important observations could be made:

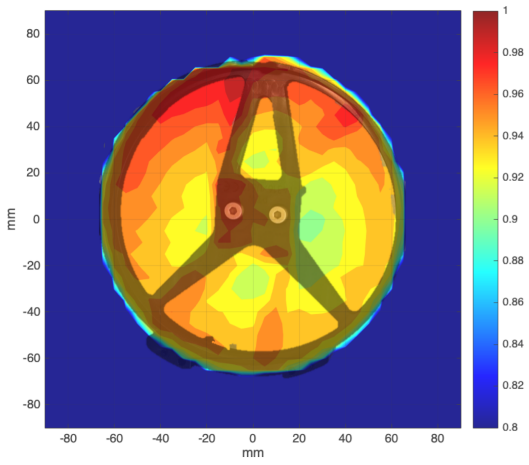

Figure 5.1: *The image of the holder superimposed on the DRM of the BPC150 acquired in photon beams*

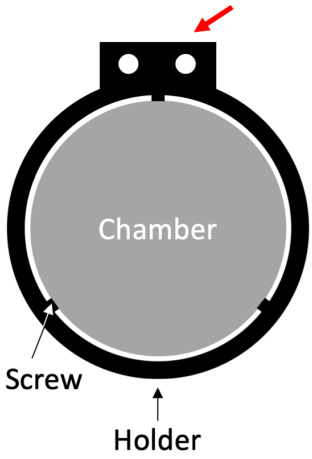

Figure 5.2: *Schematic of the holder for the chambers of type PTW34070. The red arrow marks the place, where the holder can be fixed to e.g. the movement mechanism of the water tank*

- The response maps of the PTW34070 could be given as a clear function of the radius in comparison to the DRM of the BPC150, where different regions of the active area showed a high deviation. The most likely explanation for the spotted character of the DRM of the BPC150 is X-ray back scatter caused by the holder. Figure 5.1 shows the custom made holder of the BPC150 on top of the DRM as seen in Figure 4.3b. The shape of the holder geometry is visible on the response map. Recording the DRM with different kV settings could confirm and possibly lead to a correction caused by the back scatter of the holder, as the back scatter is a function of the energy.

- The trend of the response was reversed: while both the PTW34070-SN118 and SN124 showed the highest relative response in the center, with a decrease towards the chambers edge, the BPC150 showed the highest relative response at the chambers edge, with a decrease towards the center. Kuess *et al* (2017) [22] observed the same behavior for some chambers of type PTW34080 as described here for the BPC150. The PTW34070 chambers behaved equally in both studies.

Visualizing the holder due to back scatter on the DRM was an unwanted side effect. This effect was not observed for the DRMs of the chambers of type PTW34070, as those chambers have a different type of holder. A schematic representation is provided in Figure 5.2. For the DRM of the BPC150 acquired in proton beams the back scatter of the holder was negligible. The spot size was larger for protons than for the collimated X-ray beam. Thus due to limited resolution a differing response as shown in Figure 4.6 is possible, as smaller areas with different response could potentially be overlooked.

The opposing response behavior of of the BPC150 compared to the PTW34070, especially at the chamber center, had a noticeable effect. During all measurements in IR1, the chambers were aligned in the isocenter, thus the beamlet was incident on the center of the chamber. In Table 4.8 the DAP gathered with a single beam showed a higher result when measured with chambers of type PTW34070. Although a DRM of PTW34070-SN125 was not recorded during the scope of this work, Kuess *et al* (2017) [22] stated that the chambers PTW34070 SN125 had an over response in the chamber's center of 3.2%. The difference of the DAP between BPC150 and PTW34070 SN125 measured in this work was 8%. Thus, the under response in the center of the BPC150 should be around 5%. This was confirmed by the response maps for the BPC150 taken in proton beams.

A non-uniform response of large area ionization chambers can potentially affect IDD measurements. As the spot size increases with depth, the share of the chamber's active area that is irradiated increases as well. Over a depth of 300 mm the FWHM of a proton beam in water with 252.7 MeV increases from 6.8 mm to 14.5 mm according to Monte Carlo simulations. From the response maps presented in Kuess *et al* [22] a maximum difference between IDDs curves of 2% at a depth of 300 mm were expected. However, this difference referred to two chambers with nearly 10% over- and under response in the center. Thus, this effect is expected to be below 1% for the BPC150. The impact regarding the measurement of R_{80} is however negligible. Also, carbon ion range measurements performed in the scope of this thesis (Table 4.12) showed maximum deviations of R_{80} of 0.2% between the BPC150 and the PTW34070.

The two measurements used to create the DRM of the PTW34070 SN124 showed a high standard deviation of 3.76% (SN118: 0.25%; BPC150: 0.87%). An inadequate warm-up of the tube of the X-ray tube or an overheating can be excluded, as both the outside and inside temperatures were well within the working tolerance of the tube. A closer look at the distribution of all standard deviations of the SN124's DRM showed that the highest values were

close to the chamber edge, where the response is diminished. Although the setup was not touched between measurements, an initial positioning inaccuracy potentially caused the high uncertainty. The manual for the MP3-P water phantom ([24]) states a positioning inaccuracy of 0.5 mm. The spot FWHM is 2.455 mm. Thus, about 20% of the beam could be cut off, or added due to this misalignment.

For the Hartman method an adequately large field is required to incorporate the whole active area of the chamber and to guarantee secondary charged particle equilibrium. The active diameter of the BPC150 is 147 mm. Therefore, the 15 cm $\times$ 15 cm field (see results in Chapter 4.5) just barely covered the whole active area. Thus, parts of the active area were not irradiated if the chamber was not positioned correctly at the isocenter. Additionally, secondary charged particle equilibrium could not be guaranteed, as the detector dimensions were similar to the chosen field size (see Chapter 1.8). This was reflected in the results, as the DAP measured with the 15 cm $\times$ 15 cm field deviated by 1.024% from the 19 cm $\times$ 19 cm field. The deviation between the 18 cm $\times$ 18 cm field and the 19 cm $\times$ 19 cm field was 0.005%. Thus, the recommended field size for cross calibration and DAP_{HM} measurements is 18 cm $\times$ 18 cm or larger.

The DAP measurements with the Hartman method showed a good agreement over all chambers, with a highest deviation of 2.02% between the BPC150 measured in April and the PTW34070-SN124. The lowest deviation was present between the PTW34070-SN124 and SN125 with 0.05%. Including only the measurements done in August, the highest deviation was again between the BPC150 an the PTW34070-SN124 (1.49%). For a review of the results see Table 4.7 and 4.8.

Measuring the DAP for pencil beams using LAICs is thoroughly adressed in e.g. by Palmans *et al* ([2]), Dufreneix *et al* ([20]) and Gomà *et al* ([45]). The high deviation between the Hartman and the SB method requires further investigation. During work on this MSc thesis deviations of up to 8.71% (for the BPC150) between those two methods were observed. The lowest deviation was 2.03% (PTW34070 SN125). For details see Table 4.7 and 4.8. A possible reason for those discrepancies is the non-uniformity [22]. The already mentioned response trends of the chambers (highest in the middle and decreasing towards the chamber edge for the PTW34070 and reversed for the BPC150) was reflected in the calculated k_{NU} factors for a 13.63 mm spot incident on the chamber center. The k_{NU} factors calculated in

Kuess *et al* [22] were 0.969 for the chambers SN118 and SN125. This was confirmed in this work, as the measured values differed by max. 0.5%, which is within the uncertainty given by Kuess *et al* [22].

At MedAustron a beam dose delivery system assures that the delivered number of particles per spot is in agreement to the nominal plan parameters. During this work the beam was not degraded, which is in contrary to the clinical settings, where a beam degradation of 80% is applied. Thus, it was necessary to check if the beam dose delivery system performs accurate for non-degraded beams for the applied NPS. For the SB method, the NPS was varied to investigate the expected linearity of the dose delivery system. The DAP normalized to the NPS showed a deviation within measurement uncertainty, thus it could be excluded that the deviation between DAP_{HM} and DAP_{SB} is due to a non-linearity concerning the NPS incident on the chamber.

Table 4.7 and 4.8 show, that the DAP measured with the Hartman method always exceeded the single beam method. For the investigated chambers of type PTW34070 the DAP measured with a single beam should be higher, due to the over response in the center. Therefore, the results for the DAP measured with these two methods cannot be corrected with just the calculated k_{NU} factors. The DAP_{HM} could be higher due to unforeseen edge effects, which caused additional charge to accumulate. Note, that the relative differences between chambers was in agreement with the k_{NU} factors. Thus, a systematic uncertainty during DAP measurements is possible. For example the size of the active area, as given by the vendor, could be different to the size of chambers as used in the formalism presented by Palmans and Vatnitsky ([38]). The SB and HM would agree if the size of the chambers of type 34070 are underestimated by 4%, which equals 2 mm difference in diameter.

Applying the k_{NU} correction factors to the results gathered with the SB method reduced the deviation between the BPC150 and the PTW304070-SN124 from 5.39% to 1.46% and between the BPC150 and the SN125 from 7.65% to 1.07%. The k_{NU} factor for the SN125 was adopted from Kuess *et al* (2017) [22]. Even so, the initial deviation between the PTW34070 SN124 and 125 of 2.15% increased to 2.57% after the application of the correction factors.

The DAP measurements with varying energy provided a hint to the response behavior in the center of the chamber. Figure 4.11 shows the DAP results for different energies normalized to the highest overall DAP (PTW34070 SN125). Thus, the PTW34070 SN125 had the relative highest response, followed closely by the SN124 (-2.07% at E=62.4 MeV). The

response of the BPC150 (both measurement series averaged) showed the lowest response (-6.74% at E=62.4 MeV). The relative differences in response decreased for increasing energy with respect to the SN125 to -0.69% and 2.67% for the SN124 and the BPC150 for an energy of 252.7 MeV, respectively. The FHWM of a proton beam in 2 cm water is 6.9 mm for E=252.7 MeV. For 62.5 MeV the FWHM increased to 20.2 mm, according to Monte Carlo simulations with GATE/Geant4. So a larger part of the active area was irradiated for lower energies. This explains the larger discrepancies between chambers for lower energies, as the response behavior differs between chambers.

In further work with the BPC150, measurement of the DAP with the HM for different energies is of interest. This allows a comparison of the single beam and Hartman method for varying energies. It could lead to a better understanding of the impact of spot size and beam energy in respect to the heterogeneity of response. In this manner, even larger spot sizes could be investigated by using the range shifter to further broaden the beam. Note that in this case it will be challenging to measure the lowest available energy with a penetration depth of only 30 mm.

The energy variation measurements (see Table 4.10) showed a high difference in response for 132.0 MeV and 79.6 MeV. This was caused by the fact that for the two lowest energies (i.e 62.4 MeV and 79.6 MeV)) the Bragg peak chambers were already placed within the Bragg Peak. For higher energies the chamber was positioned in the plateau region of the IDD. At an energy of 132.0 MeV the chamber was most likely in the plateau region, whereas at an energy of 79.6 MeV the chamber was located somewhere in the proximal region of the Bragg Peak.

Between the two DAP measurement series of the BPC150 the results differed by 2.07%. This is most likely due to positioning discrepancies. The distance to the entrance window of the water tank was checked with a special spacer. However, with the custom made holder of the BPC150 a perfect alignment of the chamber perpendicular to the beam was challenging. Furthermore, no dose monitor chambers were used in this measurement as these were not reference dosimetry measurements. Thus, deviations of MAPTA regarding the absolute dose have to be considered. For clinical irradiations a maximum differences in absolute dose to water of 1% is allowed. However, the quality assurance in the research room does not follow such strict procedures and a higher deviation is possible.

Measuring carbon ion IDDs with the BPC150 is maybe its most important field of application. The contribution of dose in the fragmentation tail is due to secondary particles, such as protons, helium, lithium, beryllium, boron, nitrogen and oxygen [46]. Fragmentation particles are able to travel far from the Bragg Peak position before being absorbed (e.g. up to 30 cm longitudinally for an initial beam energy of 400 MeV) [47]. Although most fragments are scattered in the forward direction, they can be dispersed in each direction, whereas a cone with an opening angle of around 50 degrees is most likely [48] [49]. Thus, the differences in response of the different chambers after the Bragg Peak (see Figure 4.13) are assumed to be related to the wider lateral distribution of the lighter fragmentation particles. As the larger active area of the BPC150 allows for a detection of more of the scattered fragments, the BPC150 seems well suited for measuring the complete carbon fragmentation. In this work 7.5% more dose was measured with the BPC150 at the beginning of the fragmentation tail in comparison to the type 34070.

Differences of 1-2% were also observed in the proximal region of the Bragg peak which might not be negligible with respect to measuring beam parameters for the treatment planning beam model.

The DRMs were acquired in air, whereas the DAP measurements were done in water. Water pressure could reduce the distance between the entrance window and the collecting electrode. This effect was investigated by Kuess *et al* [50] where DRMs were gathered in air and a water filled perspex tank and no significant difference in response was observed. However, due to the larger spot size in water and the subsequently lower resolution, minor response differences due to the water pressure might be concealed.

Additionally, due to the interaction with water the proton beamlet broadens substantially. Thus, a larger spot size as for measurements in air could was lead to a change in k_{NU} factors.

Difficulties with the BPC150's holder were versatile. Starting with the back scatter during the recording of the DRMs in photon radiation, to the issues with the chamber being tilted. Attempts to correct for the tilt of the chamber were to insert paper gauges (during air measurements) and metal gauges (during measurements in water) and to check the angle of the chamber with a water level. A holder similar to the one for type 34070 would be beneficial.

6 Conclusion and Outlook

The aim of this work was to investigate the prototype Bragg Peak chamber from PTW (BPC150) with an active diameter of 147 mm. The plane parallel ionization chamber with the largest active area is currently the Stingray from IBA (IBA Dosimetry, Schwarzenbruck, Germany), with an active diamter of 120 mm. Due to their higher collecting efficiency, LAIC's with a larger active diameter are promising. This work represented the first user test of the PTW prototype chamber. The behavior of this chamber was thoroughly tested in ^{60}Co beams, x-rays , proton, and carbon ion beams.

During the cross calibration procedure in ^{60}Co and proton beams, minor deviation from IAEA-TRS-398 guidelines were necessary. The calibration factors gathered were used to calculate the beam quality correction factor k_{Q_{cross},Q_0} of 0.98 for the BPC150.

The water equivalent thickness of the BPC150 in proton beams was assessed for the whole chamber (11.24 mm) and for its entrance window (4.63 mm).

The homogeneity response correction was found to be more important for the BPC150, due to its much larger active diameter, than for smaller LAICs, although all investigated chambers show response fluctuations of up to 10%. The trend of response for the BPC150 showed the relative lowest response in the chamber center, which was increasing radially outwards. The PTW34070 chambers showed the opposite behavior. The DRM of the BPC150 gathered in photon beams differed from the one acquired in proton beams and also from the ones of the PTW34070. The DRM of the BPC150 cannot be given as a clear function of the radius, whereas for the other chambers this was possible. This behavior is most likely caused by X-ray back scatter of the BPC150's holder.

The non-uniformity between chambers can be corrected by calculating chamber specific non-uniformity correction factors (i.e. k_{NU}). By doing so the deviation between DAP_{SB} results can be reduced from a deviation of 7.65% to 1.07%. DAP_{HM} measurements showed a good reproducibility for all investigated chambers with the highest deviation of 2.02% between the between the BPC150 (first measurement series) and the PTW34070-SN124.

However, the discrepancy between the DAP results measured with the SB and the Hartman method need further investigations to clarify the systemtic offset of about 4%.

The custom made holder of the BPC150 presented some challenges regarding x-ray back scatter and alignment of the chamber.

Further work with the BPC150 will include DAP_{HM} measurements with different energies and comparing those to DAP_{SB} measurements with deliberately broadened spots (range shifter). Furthermore, comparison of the BPC150's behavior to the IBA Stingray is enticing. Comparison of the measurements with Monte Carlo simulations should be performed. Additionally, recording DRMs with other LAICs from different brands than PTW would be interesting.

List of Figures

List of Tables

Bibliography

[1] W R Hendee, G S Ibbott, and E G Hendee. *Radiation therapy physics*. John Wiley & Sons, 2013. 2, 7, 9, 11, 14, 83

[2] H Palmans, P Andreo, K Christaki, MS Huq, and J Seuntjens. Dosimetry of small static fields used in external beam radiotherapy: an iaea-aapm international code of practice for reference and relative dose determination. *International Atomic Energy Agency, Vienna*, 2017. 3, 19, 20, 77, 83

[3] J Wuerfel. Dose measurements in small fields. *Med Phys*, 1(1):81–90, 2013. 3, 19

[4] H Bagheri, A Soleimani, N Gharehaghaji, A Mesbahi, F Manouchehri, B Shekarchi, B Dormanesh, H A Dadgar, et al. An overview on small-field dosimetry in photon beam radiotherapy: Developments and challenges. *Journal of cancer research and therapeutics*, 13(2):175, 2017. 3, 19

[5] E Richter and T Feyerabend. *Grundlagen der Strahlentherapie*. Springer-Verlag, 2013. 3, 4, 7, 26

[6] W Demtröder. *Experimentalphysik 2: Elektrizität und Optik*. Springer-Verlag, 1995. 3

[7] J T Bushberg. The aapm/rsna physics tutorial for residents. x-ray interactions. *Radiographics*, 18(2):457–468, 1998. 4, 5, 83

[8] W Demtröder. *Experimentalphysik 3: Atome, Moleküle und Festkörper*. Springer-Verlag, 2016. 4

[9] W Demtröder. *Experimentalphysik 4: Kern-, Teilchen-und Astrophysik*. Springer-Verlag, 2004. 4

[10] H Krieger. *Grundlagen der Strahlungsphysik und des Strahlenschutzes*. Springer-Verlag, 2009. 4, 7, 26

[11] Wayne D Newhauser and Rui Zhang. The physics of proton therapy. *Physics in medicine and biology*, 60(8):R155, 2015. 7

[12] E B Podgorsak et al. Treatment machines for external beam radiotherapy. *IAEA Radiaon Oncology Physics: A Handbook for Teachers And Students Internaonal Atomic Energy Agency, Vienna*, 2005. 11, 83

[13] H Paganetti. *Proton Beam Therapy*. 2399-2891. IOP Publishing, 2017. 14

[14] R L Maughan, M J Hardy, M J Taylor, J Reay, and R Amos. Radiation shielding and safety for particle therapy facilities. In *Design and Shielding of Radiotherapy Treatment Facilities*, 2053-2563, pages 11–1 to 11–42. IOP Publishing, 2017. 14, 15, 16, 83

[15] R Leroy, N Benahmed, F Hulstaert, F Mambourg, N Fairon, E Van Eycken, and D De Ruysscher. Hadron therapy in children – an update of the scientific evidence for 15 paediatric cancers. *Health Technology Assessment (HTA) Brussels: Belgian Health Care Knowledge Centre (KCE)*, 2015. 16, 83

[16] M Benedikt and A Wrulich. Medaustron—project overview and status. *The European Physical Journal Plus*, 126(7):69, 2011. 17

[17] M Stock, D Georg, A Ableitinger, A Zechner, A Utz, M Mumot, G Kragl, J Hopfgartner, J Gora, T Böhlen, et al. The technological basis for adaptive ion beam therapy at medaustron: status and outlook. *Zeitschrift für Medizinische Physik*, 2017. 17

[18] P Andreo, DT Burns, K Hohlfeld, M Saiful Huq, T Kanai, F Laitano, V Smyth, and S Vynckier. Iaea trs-398. absorbed dose determination in external beam radiotherapy: an international code of practice for dosimetry based on standards of absorbed dose to water. *International Atomic Energy Agency*, 2000. 18, 35, 36, 39, 73

[19] R Alfonso, P Andreo, R Capote, M Saiful Huq, W Kilby, P Kjäll, TR Mackie, H Palmans, K Rosser, J Seuntjens, et al. A new formalism for reference dosimetry of small and nonstandard fields. *Medical physics*, 35(11):5179–5186, 2008. 19, 21

[20] S Dufreneix, A Ostrowsky, M Le Roy, L Sommier, J Gouriou, F Delaunay, B Rapp, J Daures, and JM Bordy. Using a dose-area product for absolute measurements in small fields: a feasibility study. *Physics in Medicine & Biology*, 61(2):650, 2015. 19, 21, 77

[21] I J Das, G X Ding, and Anders A. Small fields: nonequilibrium radiation dosimetry. *Medical physics*, 35(1):206–215, 2008. 19, 20, 83

[22] P Kuess, T T Böhlen, W Lechner, A Elia, D Georg, and H Palmans. Lateral response heterogeneity of bragg peak ionization chambers for narrow-beam photon and proton dosimetry. *Physics in Medicine & Biology*, 62(24):9189, 2017. 21, 43, 44, 75, 76, 77, 78

[23] Yxlon International GmBH. *Betriebsanleitung Y.Solution Maxishot*, 2013. 23

[24] PTW Freiburg. *Assembly Instructions and User Manual: MP3-P Therapy Beam Analyzer T41029, PT Water Reservoir T41028*, 2016. 26, 77, 85

[25] PTW Freiburg. *Assembly Instructions and User Manual MP3-PL Therapy Beam Analyzer T41050*, 2016. 26, 85

[26] PTW Freiburg. *User Manual: Bragg Peak Chambers Type 34070, 34073 and 34080*, 2009. 27, 29, 38, 85

[27] PTW Freiburg. *User Manual Roos Chamber Ionization Chamber Type 34001*, 2015. 27, 29, 85

[28] PTW Freiburg. *Farmer Chamber Ionization Chamber Type 30010, 30011, 30012, 30013*, 2016. 29, 30, 83

[29] PTW Freiburg. *User Manual: UNIDOSwebline Type 10021, Type 10022 and Type 10023*, 2014. 31

[30] PTW Freiburg. *TANDEM T10011, T10015 and T10016 TANDEM XDR T10037, T10038 and T10039*, 2013. 31

[31] PTW Freiburg. *TBA CONTROL UNIT*, 2015. 31

[32] PTW Freiburg. *PEAKFINDER Water Column T41030 with SERVO CONTROL UNIT T41027*, 2014. 31

[33] D Georg, M Stock, H Fuchs, B Knäusl, P Kuess, and T Schreiner. Abnahmebericht nichklinischer strahlungsraum ir1. Technical report, MedAustron, Wiener Neustadt, Austria, 2016. 32, 48

[34] A De Franco, TT Böhlen, F Farinon, G Kowarik, M Kronberger, C Kurfürst, S Nowak, F Osmić, M Pivi, C Schmitzer, et al. Upgrade study of the medaustron ion beam center. In *IPAC2017, Copenhagen, Denmark, paper THPVA074, this conference*, 2017. 32

[35] S Giordanengo, MA Garella, F Marchetto, F Bourhaleb, M Ciocca, A Mirandola, Vincenzo Monaco, MA Hosseini, Cristiana Peroni, Roberto Sacchi, et al. The cnao dose delivery system for modulated scanning ion beam radiotherapy. *Medical physics*, 42(1):263–275, 2015. 32

[36] PTW Freiburg. *RW3 Slab Phantom T29672 and T40006.1.001*, 2015. 34, 36

[37] GH Hartmann, O Jäkel, P Heeg, CP Karger, and A Kriessbach. Determination of water absorbed dose in a carbon ion beam using thimble ionization chambers. *Physics in Medicine & Biology*, 44(5):1193, 1999. 40

[38] H Palmans and S M Vatnitsky. Beam monitor calibration in scanned light-ion beams. *Medical physics*, 43(11):5835–5847, 2016. 42, 78

[39] S Seo. *A review and comparison of methods for detecting outliers in univariate data sets*. PhD thesis, University of Pittsburgh, 2006. 51

[40] C Bäumer, B Koska, J Lambert, B Timmermann, T Mertens, and P T Talla. Evaluation of detectors for acquisition of pristine depth-dose curves in pencil beam scanning. *Journal of applied clinical medical physics*, 16(6):151–163, 2015. 73

[41] N Mojżeszek, M Kłodowska, W Komenda, L Stolarczyk, R Kopeć, and P Olko. Geometrical efficiency of plane-parallel ionization chambers in proton scanning beam. *Radiation protection dosimetry*, 180(1-4):334–337, 2017. 73

[42] T Hanušová, K Johnová, M Navrátil, J Valenta, and L Müller. Activation of qa devices and phantom materials under clinical scanning proton beams—a gamma spectrometry study. *Physics in Medicine & Biology*, 63(11):115014, 2018. 73

[43] C Gomà, B Hofstetter-Boillat, S Safai, and S Vörös. Experimental validation of beam quality correction factors for proton beams. *Physics in Medicine & Biology*, 60(8):3207, 2015. 73, 74

[44] J Sorriaux, M Testa, H Paganetti, D Bertrand, J A Lee, H Palmans, S Vynckier, and E Sterpin. Consistency in quality correction factors for ionization chamber dosimetry in scanned proton beam therapy. *Medical physics*, 44(9):4919–4927, 2017. 74

[45] C Gomà, S Safai, and S Vörös. Reference dosimetry of proton pencil beams based on dose-area product: a proof of concept. *Physics in Medicine & Biology*, 62(12):4991, 2017. 74, 77

[46] CK Ying, D Bolst, L T Tran, S Guatelli, A B Rosenfeld, and WA Kamil. Contributions of secondary fragmentation by carbon ion beams in water phantom: Monte carlo simulation. In *Journal of Physics: Conference Series*, volume 851, page 012033. IOP Publishing, 2017. 80

[47] Z Francis, E Seif, S Incerti, C Champion, M Karamitros, MA Bernal, VN Ivanchenko, A Mantero, HN Tran, and Z El Bitar. Carbon ion fragmentation effects on the nanometric level behind the bragg peak depth. *Physics in Medicine & Biology*, 59(24):7691, 2014. 80

[48] MS Golovkov, LV Chulkov, D Schardt, DV Aleksandrov, and G Kraus. Fragmentation of 270 a mev carbon ions in water. Technical report, SCAN-9706113, 1997. 80

[49] M De Napoli, C Agodi, G Battistoni, AA Blancato, GAP Cirrone, G Cuttone, F Giacoppo, MC Morone, D Nicolosi, L Pandola, et al. Carbon fragmentation measurements and validation of the geant4 nuclear reaction models for hadrontherapy. *Physics in Medicine & Biology*, 57(22):7651, 2012. 80

[50] P Kuess, T Böhlen, A Elia, J Osorio, D Georg, and H Palmans. Impact of lateral response non-uniformity of large-area ionization chambers on proton dosimetry. unpublished, 2017. 80